HIGH FREQUENCY GROUND MOTION SCALING IN EASTERN TURKEY

by

Korhan Umut ŞEMİN

B.S., Geophysical Engineering, Istanbul University, 2001

Submitted to

Boğaziçi University

Kandilli Observatory and Earthquake Research Institute

in partial fulfillment of

the requirements for the degree of

Master of Science

in

Geophysics

Boğaziçi University

2006

ACKNOWLEDGEMENTS

I would like to thank my parents for supporting me and giving me their unconditional love through my many years of study. I thank Prof. Dr. Cemil Gürbüz, my advisor, for his support throughout this work and everything he did for me. I also thank Prof. Dr. Niyazi Türkelli for providing the excellent data set used for this research. Finally I appreciate the assistance of my friends for helping me to finish this work.

ABSTRACT

HIGH FREQUENCY GROUND MOTION SCALING IN EASTERN TURKEY

A regional study of ground motion scaling parameters is presented for the region surrounding the eastern Turkey. The data set used in this study consists of 100 earthquake events from Eastern Turkey Seismic Experiment (ETSE) network with the magnitudes between (M_L and M_w) 3.0 – 5.5. All selected events are in the upper crust. In order to emprically obtain the scaling relationships for high frequency S-wave motion, regressions are carried out on three component broadband seismograms, all recorded within a hypocentral distance of 400 km to emprically obtain the scaling relationships for the high frequency S-wave motion. The signals were processed to examine the peak ground velocity and Fourier velocity spectra in the frequency range of 0.3 - 10 Hz. Random vibration theory (RVT) is used to test estimates of the peak ground motion in the time domain. Comparison of the two regressions indicated both regression results display consistent shapes. Geometrical spreading function g(r), characterized by: $g(r) = r^{-1.0}$ for $r \leq 40$ km, r^0 is used for $40 \leq r \leq 100$ km and $r^{-0.5}$ is used for $r \geq 100$ km. A very low quality factor, $Q(f) = 50f^{0.75}$ is used to described the anelastic crustal attenuation in the region.

Excitation terms are well matched. An effective high-frequency, distance independant spectral parameter, $\kappa_{eff} = 0.035$ sec, is obtained in this study. Both regressions show that eastern Turkey region has very high attenuative properties.

ÖZET

TÜRKİYE' NİN DOĞUSUNDA YÜKSEK FREKANSLI YER HAREKETİ ÖLÇEKLENDİRMESİ

Bu çalışmada Doğu Anadolu bölgesi için yer hareketi ölçeklendirme parametreleri sunulmuştur. Büyüklükleri 3.0 ile 5.5 arasında değişen 100 adet deprem Doğu Anadolu Sismik Deneyi Sismograf Ağından alındı. Alınan bu depremler, 400 km'lik odak uzaklığı içerisinde kaydedilmişlerdir. Bütün depremler üst kabuk içerisinde meydana gelmişlerdir. Üç bileşenli bu depremlere, yüksek frekanslı S dalgası hareketinin ampirik olarak elde edilmesi amacıyla regresyon analizi uygulandı. Sinayaller 0.3-10 Hz frekans aralığında hem en yüksek yer hızını hemde Fourier hız spekturumunu incelemek üzere işleme tabi tutuldu. Zaman boyutunda hesaplanan en yüksek yer hareketini test etmek için Random Vibration Theory kullanıldı. İki faklı alandaki regresyonlar karşılaştırıldığında ikisinin de uyumlu olduğu görüldü. Modelleme sonunda elde edilen geometrik dağılma parametresi g(r) $r \leq 40$ km için $r^{-1.0}$, $40 \leq r \leq 100$ km için r^{0} ve $r \geq 100$ km için $r^{-0.5}$ olarak elde edildi. Çok düşük bir kalite faktörü $Q(f) = 50f^{0.75}$ anelastik soğurulmayı tanımlamak için seçildi. Excitation değerleri model ile iyi bir uyuşma gösterdi. Bunun sonucunda uzaklıktan bağımsız yüksek frekans efektif bir parametre olan $\kappa_{eff} = 0.035$ olarak elde edildi. Her iki regresyon sonucu gösteriyor ki Doğu Anadolu bölgesi yüksek bir soğurma oranına sahip.

TABLE OF CONTENTS

LIST OF FIGURES

LIST OF TABLES

1. INTRODUCTION

1.1 Introduction

The assessment of seismic hazard is probably the most important contribution of seismology to society. The prediction of the earthquake ground motion has always been of primary interest for seismologists and structural engineers. The need for seismic hazard studies in the Eastern Anatolia region has become progressively more important for earthquake engineering applications because of the real earthquake threat. A fundamental requirement for these studies is the determination of the ground-motion predictive relationships (Kramer, 1996). Attenuation relationships have been developed for many regions of the world (Boore, 1983; Toro and Mcguire, 1987; Boore and Joyner, 1991; Atkinson and Boore, 1995; Ambraseys, 1996; Atkinson and Silva, 1997; Campell, 1997; Sadigh, 1997) mainly by regressing data from strong motion recordings. The sparse distribution of strong motion stations and recordings in Turkey makes the gathering of a substantial set of acceleration recordings from large events and subsequent regression impossible at the present time. Another option is to extrapolate from a set of local recordings of small events. Small earthquakes can be used to completely define the attenuative properties of the crust at frequencies greater than 1 Hz. Equations giving ground motion as a function of magnitude and distance can be empirical or model based. Empirical methods require a large data set in terms of earthquake size and observation distance for regression. Model based predictions use parametric models to provide an excitation of site spectrum and duration, which is then used with a stochastic simulation of ground motion.

Ground motion at a particular site is influenced by three main elements: source, travel path, and local site conditions. Source factors include size, depth, stress drop, rupture process, and fault geometry. Travel path factors include geometrical attenuation, dissipation of seismic energy due to anelastic properties of the earth, and focusing and scattering of elastic waves by the three-dimensional earth. Local site factors include the properties of the uppermost several hundred meters of rock and soil and the effect of the surface topography near the recording site. The physical characteristics of the propagation which carries elastic energy can change. Ground motion at periods (>> 1 sec) will generally be dominated by surface waves. The fundamental-mode surface waves are affected by scattering (produced by the complexity) and intrinsic absorption of the medium as they pass through a laterally complex structure. The direct S wave carries the main shear wave energy at short distance (≤ 80 km), while the post-critical reflections of S waves, namely Lg wave, are the dominant phase at distances of 150 to 1000 km. Wave propagation in the transition distance ranging of 80 to 150 km is more complex.

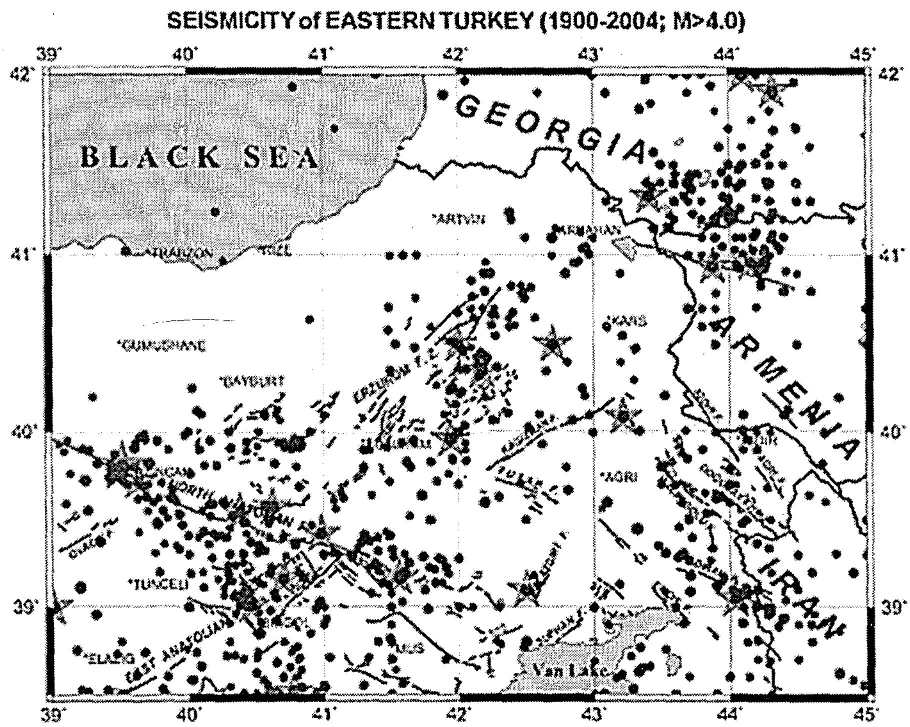

Figure 1.1. Distribution of the earthquakes with magnitudes larger than M>4.0, Green stars show the magnitudes bigger than M>6.0 earthquakes. (KOERI)

Results of the Eastern Turkey Seismic Experiment project have provided new insights for the crustal / lithospheric structure of Eastern Turkey. Studies of Pn tomographic imaging of mantle lid velocity and anisotropy by Al-Lazki et al. (2003) and regional wave propagation of Sn waves by Gok et al. (2000) have revealed that the mantle lithosphere is either very thin or completely absent beneath the region. On the other hand, crustal thicknesses gathered from the studies of receiver functions indicate almost a gradual change from <38 km in the southeast around the southern part of the Bitlis suture zone to 50 km in the north (Zor et al., 2003), averaging to some 45 km. This indicates that an almost normal-thickness crust resides on an extremely thin mantle lithosphere or perhaps almost directly on the asthenosphere. What is even more remarkable is that areas of inferred complete lithospheric detachment almost exactly coincide with the extent of the Eastern Anatolian Accretionary Complex (EAAC) (Sengor et al., 2003).

This study presents a quantitative analysis of attenuation, duration and site effects using data from a temporary three component broadband, digital seismograph network (ETSE) in Eastern Anatolia. Describing the attenuation of the ground motion as a function of frequency and hypocentral distance can be used for engineering design and seismic hazard.

For Southern California (Raoof et al., 1999), the Apennines (Malagnini et al., 2000a), and Utah (Jeon, 2000) the authors performed regressions on very large data sets obtained from regional seismic networks to focus on the propagation (attenuation) of ground motion at different frequencies. Also in Erzincan region in Turkey (Akinci et al., 2001) the distance scaling relationship is characterized by following the approach described by Raoof et al. (1999) and Malagnini et al. (2000a).The results in Erzincan region show a much more rapid decrease with the distance than the relations usually used in Turkey.

I begin in Chapter 1 with an outline of the previous studies in Eastern Turkey and objective of this study. Brief geology and tectonics are given in chapter 2. The methodology used in this study is explained in Chapter 3. The data set and data preparation steps are given in Chapter 4, Chapter 5 contains the general data regression and forward modeling of the regression. I conclude with results and general discussion in Chapter 6.

1.2 Previous studies

The Eastern Turkey Seismic Experiment (ETSE) significantly improved the station coverage in order to provide evidence of the ongoing seismic deformation. Many studies have been performed using the ETSE data. In order to provide new insights to seismogenic zones in eastern Turkey, a total number of 1165 earthquakes were located and classified into four different categories based on the reliability of the locations as established by the data covarege (Turkelli *et al.*, 2003). The accuracy of locations is estimated to be less than approximately 5 km. Arrival times of both Pg and Sg or Pn and Sn phases were obtained by visual inspection and manually picked. Results show that eastern Anatolia has higher seismic activity than previously documented. They found no subcrustal earthquakes recorded beneath the Arabian-Eurasian collision zone which suggests no or very little underthrusting of the Arabian plate beneath Eurasia.

ETSE results show that, seismic activity in this region is higher than previously observed due to number of stations. Also accuracy of hypocenter locations is significantly improved. Most of the seismic activity occurs in the upper crust between depth ranges 2-10 km. The deepest event recorded was 32km which is located on the Bitlis suture zone.

Using teleseismic recordings, receiver function analysis was performed in order to investigate the crustal structure of the Anatolian plateu in Eastern Turkey (Zor, 2003). The three component recordings of teleseismic events from a wide range of epicentral distances (25-90) were used to obtain single event receiver functions. Receiver functions were analyzed in order to obtain S wave velocity structure. The results show that the crust thickens from 42 km near the southern part of the Bitlis suture zone to 50 km along the northern edge of the Anatolian plateau in the vicinity of the North Anatolian Fault. In the east, crustal thickness increases in the northern Arabian plateau from 40km to 46-48km in the middle of the Anatolian plateau. A low velocity zone was found in the crust beneath the middle part of the array where the crustal thickness is around 46-48 km.

During the study of the propagation characteristics of regional shear waves, Sn and Lg, have been used to constrain lithospheric structure and provide insights into the ongoing tectonics of the Eastern Anatolia (Gok, 2003). Regional earthquakes within the distance range of 2-15 degrees were used. The propagation efficiencies of Sn and Lg phases were examined and ranked by their amplitude and frequency content. Attenuation maps are then tomographically constructed using the ranks of propagation efficiency. Results show that Sn is not observed in Eastern Turkey while highly attenuated for paths that cross the Dead Sea Fault Zone. Efficient Sn along the Zagros fold and thrust belt has been observed. Their results are consistent with there being a region of thin hot lithospheric mantle beneath the Anatolian and Iranian plateaus. They observed Lg to be less efficient in the relatively stable Arabian platform and for paths that cross the Dead Sea fault zone. Lg is blocked throughout the northeastern Anatolia Plateau where there may be partial melt in the crust due to the wide spread volcanism in the region.

In the Pn phase attenuation study, Pn wave velocity and anisotropy beneath the Arabian, Eurasian and African plates' junction have been mapped (Al-Lazki, 2003). Two types of low Pn velocity anomalies have been found. A broader scale (~500 km) low Pn velocity zone (< 8.0 km/s) underlies regions within and nearby the Arabian plate boundaries and beneath most of the Anatolian plate. Smaller scale (~200 km) very low Pn velocity (< 7.8 km/s) zones were found to underlie the Lesser Caucasus, southern Syria and northern Jordan, the Isparta Angle, central Turkey and the northern Aegean Sea back arc region. At the northern and northeastern boundaries of Arabia the low velocity zone underlies regions parallel and northeast of the Zagros and north of the Bitlis sutures. In contrast, at the northwestern boundary of Arabia the low velocity zone underlies the Dead Sea Fault (DSF) system and the northwestern Arabian plate. They interpreted the northwestern Arabia broad anomaly and the very low smaller anomaly within Syria, Jordan and nearby regions as part of the Red Sea and East Africa rift system. The broad low velocity zone beneath Iran, Eastern Turkey and the Anatolian plate may be in part the result of subducted Tethyan oceanic lithosphere beneath Eurasia. High Pn velocities (8.1 - 8.4 km/s) underlie the Mediterranean Sea, the southern Aegean Sea, the Black Sea, the southern Caspian Sea extending eastwards under the Kopeh Dagh and westwards under Azerbaijan, eastern Romania, and central and the eastern Arabian plate. The extent of high Pn velocity of central and eastern Arabia across the Bitlis and Zagros suture lines is used to infer the possible underthrusting of the Arabian plate beyond the suture lines. Along the southern Zagros the high Pn velocity zone extends beyond the suture line, this may be indicative of Arabia underthrusting parts of the Sanandaj-Sirjan region of western Iran. In contrast, the lack of high Pn velocity beyond the Bitlis suture line implies limited underthrusting of Arabia beyond the Bitlis suture. Observed Pn anisotropy showed a higher degree of lateral variations in comparison to Pn velocity. In eastern Anatolia, where they observed a localized very low Pn velocity zone. The mapped Pn azimuthal anisotropy also showed coherency in orientations in the same zone. Moreover, the Pn anisotropy orientations were similar to observed orientations of polarization anisotropy based on shear wave (SKS) splitting analysis (Sandvol, 2003). This implies a thinned or absent mantle lid in eastern Anatolia and that Pn anisotropy and SKS splitting are both sampling asthenospheric deformation.

Shear-wave splitting analysis (Sandvol, 2003) indicates that there is no significant change in upper mantle polarization anisotropy across the Bitlis suture or the EAFZ. There also appears to be some correlation between very slow mantle lid velocity and large splitting lag times across the eastern portion of the Anatolian plateau.

1.3 Objective of the study

The objective of this study is the quantative description of the regional attenuations of the earthquake related high frequency ground motion in eastern Turkey. To predict the amplitude of a future strong ground motion, we need to understand the regional variations in attenuation. Describing the attenuation of the ground motion as a function of frequency and hypocentral distance can be used for engineering design and seismic hazard.

2. GEOLOGY AND TECTONICS

2.1 Tectonics

The East Anatolian High Plateau is a region of average ~2 km elevation exhibiting active diffuse N-S shortening and widespread Pliocene to recent volcanism. Its elevation was hitherto thought to result from a presumed crustal thickness of about 55 km. Seismic data collected by ETSE have shown, however, that its crustal thickness is only some 45-48 km. Combined with tomographic models of regional seismic velocity and attenuation, this shows that most of the East Anatolian High Plateau is devoid of mantle lithosphere. The absence of mantle lithosphere is ascribed to break-off of northward subducted slab beneath the prism and the widespread volcanism to melting its lower levels because of direct contact with hot asthenosphere. The East Anatolian High Plateau is thus supported not by thick crust, but by hot mantle.

The Bitlis suture/thrust zone and the East Anatolian fault system (EAF) mark a distributed, irregular, and young continental collision zone. The Northward motion of the Arabian plate relative to Eurasia causes lateral movement and rotation of the Anatolian block to the west, as evidenced by the right-lateral strike-slip movement along the North Anatolian fault system (NAF) (Sengor, 1979; Dewey and Sengor, 1979; McCluskey at al., 2000) and the left lateral strike-slip movement along the EAF (McKenzie, 1972; Jackson and McKenzie, 1988). The Anatolian block is escaping westward due, in part, to the northward motion of the Arabian plate. The NAF and EAF have been active since the Miocene (e.g., Allen, 1975; Ambraseys, 1970; Barka and Kadinsky-Cade, 1988) and are associated with large pull apart basins, such as the Karliova basin located at the junction of these two fault systems (Hempton, 1985). The area to the east of Karliova triple junction is characterized by an N-S compressional tectonic regime and conjugate strike slip faults of dextral and sinistral character, mostly paralleling the NAF and EAF which are the dominant structural elements of the region.

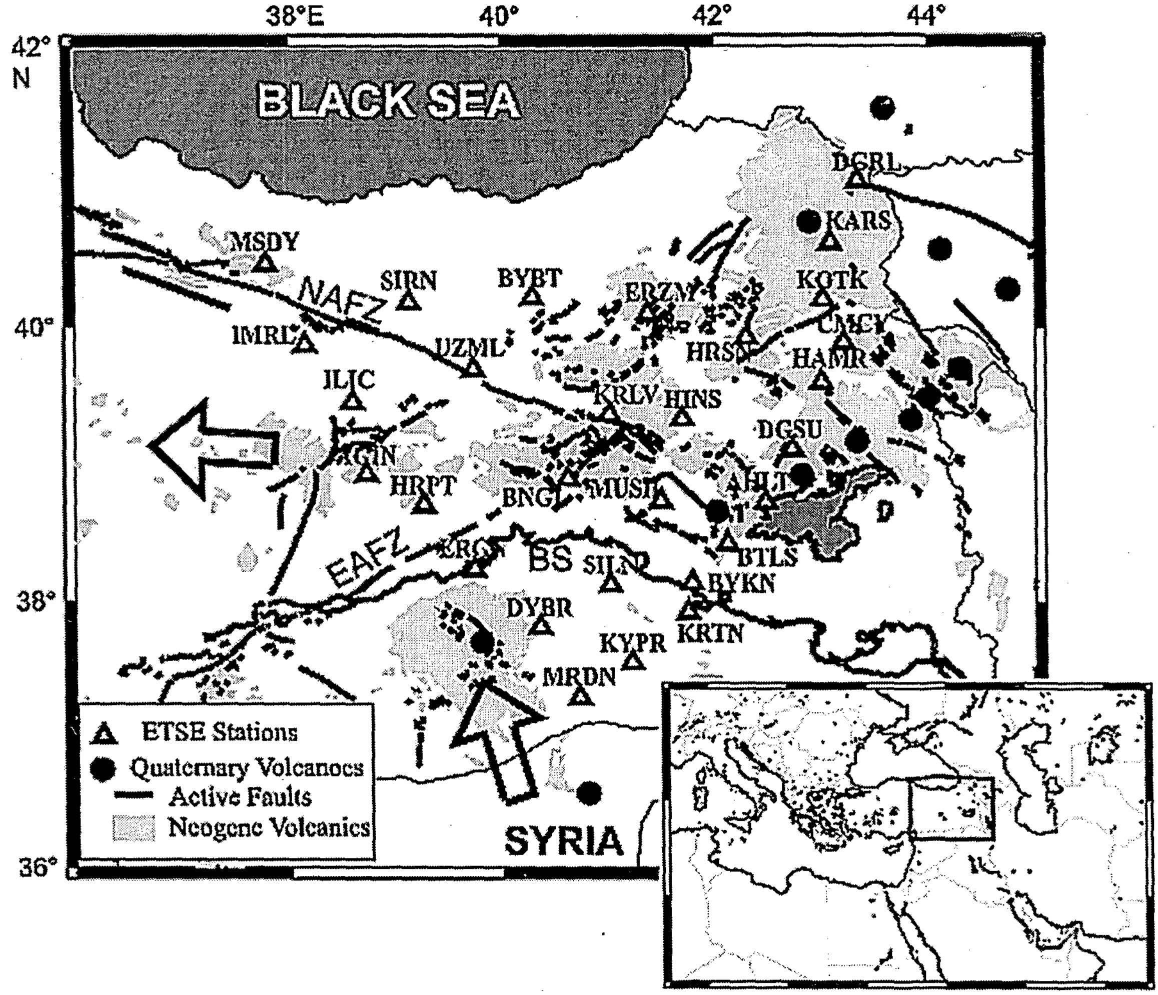

Figure 2.1: Map showing the 29 three-component PASSCAL broadband stations (triangles) used in the ETSE. Filled circles indicate Quaternary volcanoes and the gray shaded area shows Neogene volcanics. Arrows indicate the direction of the plate and fault motions. BS, NAFZ, and EAFZ are the Bitlis-Zargos suture zone, North Anatolian fault zone, and East Anatolian fault zone, respectively. [Zor et al., 2003]

2.2 Geology

The Anatolian – Iranian Plateau extends from Eastern Anatolia to Eastern Iran, and typically has an elevation of about 1.5 – 2 km in Eastern Anatolia. The basement of the Anatolian – Iranian Plateau is made up of micro-continents, accreted to each other during the Late Cretaceous to Early Tertiary. These micro-continents are separated from each other by ophiolite belts and accretionary complexes. Five different tectonic blocks are recognized in North-Eastern Anatolia (Fig. 2.2); The Eastern Rhodope-Pontide fragment in the northwest of the region (I in Fig. 2.2). It underlies the south-western and north-eastern parts of the Erzurum Kars Plateau (i.e. EKP in Fig. 2.2). The Northwest Iranian fragment (II in Fig. 2.2). The eastern part of the Erzurum-Kars Plateau (i.e. Horasan, Aladag, Kagizman, Kars areas and Mt. Ararat) overlies this tectonic block (Keskin et al., 1998), The Eastern Anatolian Accretionary Complex in the middle of the region located between the Aras River and the Bitlis-Zagros Thrust and fold belt (III in Fig.2.2), The Bitlis-Zagros unit which is exposed along the Taurus belt (IV in Fig.2.2), and Autochthonous units of the Arabian continent or foreland (V in Fig.2.2). Except for the EAAC, all the tectonic blocks correspond to the aforementioned micro-continents.

The Eastern Rhodope-Pontide unit is located in the northernmost part of the region. Its basement is represented by a metamorphic massive named the Pulur Complex (Topuz et al., 2004). The Pulur complex is composed of a heterogeneous set of granulite facies rocks, ranging from quartz-rich mesocratic gneisses to silica- and alkali-deficient, Fe-, Mg- and Al-rich melanocratic rocks (Topuz et al., 2004). A thick volcano-sedimentary arc sequence overlies this metamorphic basement. This sequence is regarded as an ensialic, south-facing magmatic arc, formed by north-dipping subduction under the Eurasian continental margin (Yilmaz et al., 1997) in a period between the Albian and Oligocene (Sengor et al., 2003).

The Northwest Iranian fragment is masked by collision-related volcanic units in Eastern Anatolia. It is exposed in Armenia around the Tsakhkuniats basement outcrop and Hankavan-Takarly and Agveran massifs (Karapetian et al., 2001). The unit is composed of a heterogeneous rock sequence, consisting of trondhjemitic, phyillitic, albite-plagiogranitic, plagiogranite- and granite-migmatitic lithologies (Karapetian et al., 2001).

The Eastern Anatolian Accretionary Complex (EAAC) forms a 150-180 km wide, NW-SE extending belt in the middle of the region. It represents the remnant of a huge subduction-accretion complex formed on a north-dipping subduction zone located between the Rhodop-Pontide in the north and the Bitlis-Zagros microcontinent in the south in a period between the Late Cretaceous and Oligocene (Sengor et al., 2003). It consists of two contrasting rock units:

An ophiolitic melange of Late Cretaceous age, and Paleocene to Late Oligocene flysch sequences incorporated into the ophiolitic melange as north-dipping tectonic slices. These flysch slices become younger from north to south and shallower from the Cretaceous to the Oligocene (Sengor et al., 2003). This observation is consistent with the polarity of the subduction zone that is thought to have created the Eastern Anatolian accretionary prism by underthrusting.

The Bitlis-Zagros Thrust and fold belt is exposed in a NW-SE extending belt along the Eastern Taurus mountain range. It is regarded as the easternmost extremity of the Menderes-Taurus block. It consists of medium-to-highly metamorphosed units.

Shallow marine deposits of Oligocene to Middle Miocene age unconformably overlie these tectonic blocks in some places (not shown in Figs. 2.2 and 2.1). Collision-related volcanic units, on the other hand, unconformably overlie both these five tectonic blocks and the aforementioned marine deposits, masking the basement units over great distances (Figs. 2.2, 2.3).

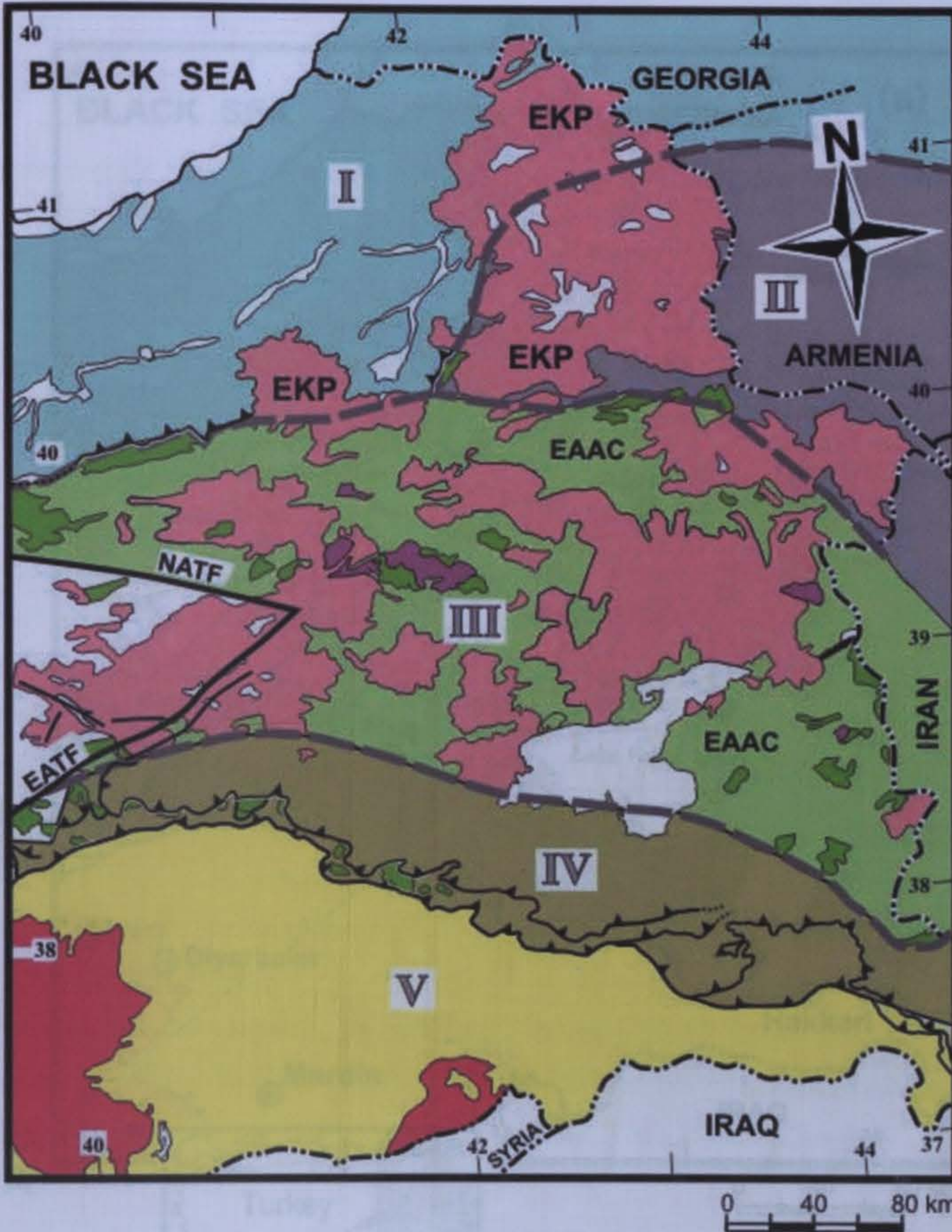

Figure 2.2. Major tectonic blocks of the Eastern Anatolia region[Keskin, 2003]. The borders are modified from Sengor et al. (2003). I: Rhodope-Pontide fragment, II: Northwest Iranian fragment, III: Eastern Anatolian Accretionary Complex (EAAC), IV: Bitlis-Zagros Thrust and fold belt, V: Arabian foreland. Dark green areas: outcrops of ophilitic melange, Pink and red areas: collision-related volcanic units, white areas: undifferentiated units or young cover formations. EKP: the Erzurum-Kars Plateau in the north.

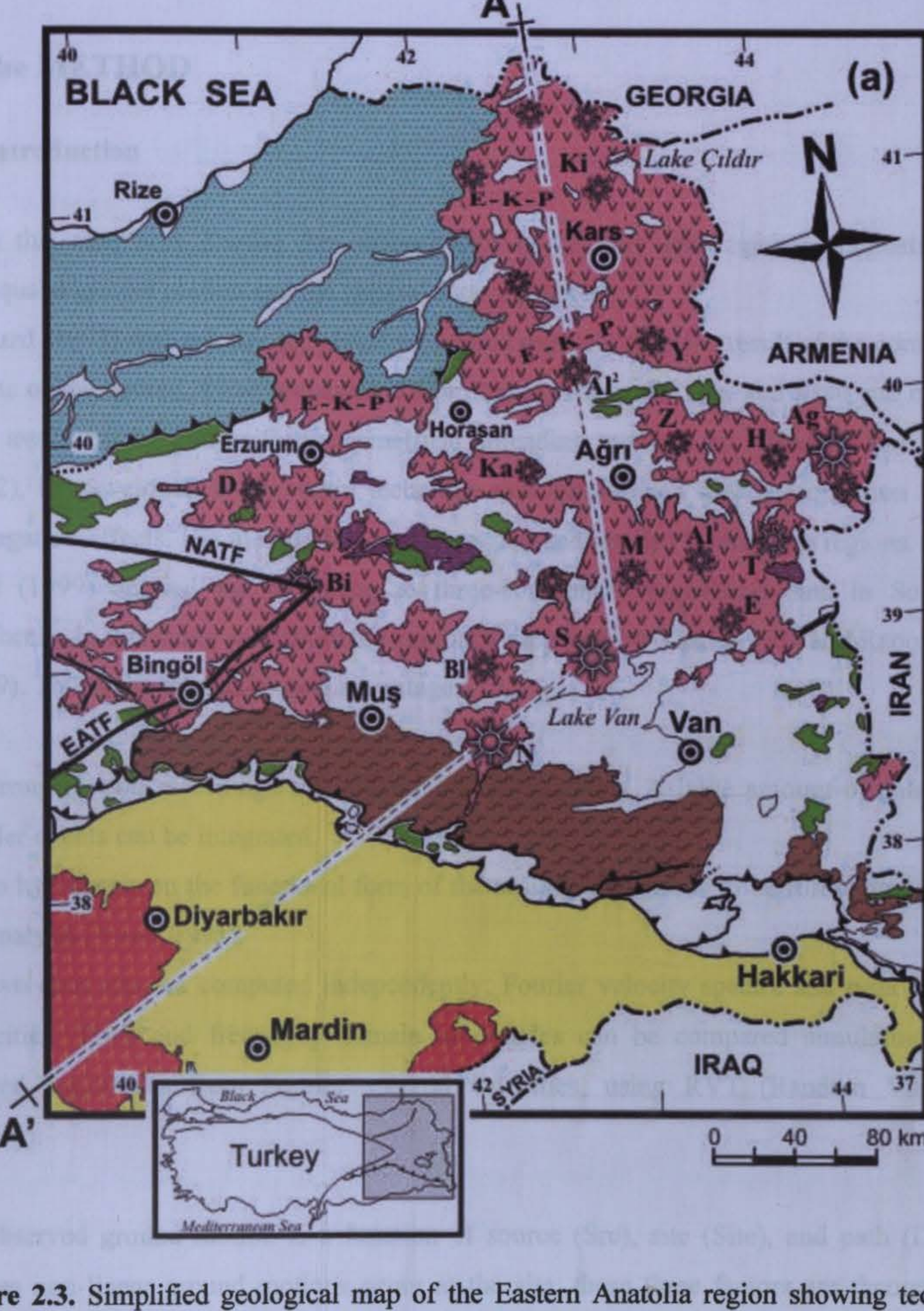

Figure 2.3. Simplified geological map of the Eastern Anatolia region showing tectonic units, collision-related volcanic products and volcanic centers (compiled by Keskin, 2003). E-K-P: the Erzurum-Kars Plateau; NATF and EATF: North and East Anatolian Transform Faults.[Keskin, 2003]

3. The METHOD

3.1 Introduction

In this chapter I discuss the methodology to quantify the regional attenuation of earthquake ground motion and the general data regression.

Yazd (1993) realized that the observed ground motions were the result of the composite effects of the source, wave propagation from the source to the site, and local site effects. Also aware of the non-uniform geometrical spreading required by Atkinson and Mereu (1992), he developed a regression technique that emphasized the determination of the propagation effects. His method has been extended and applied to different regions. Raoof et al (1999) applied the technique to three-component broadband data in Southern California. In this study we follow the approach proposed by Yazd (1993) and Raoof et al. (1999). This approach has several advantages:

1. Strong motion recordings are not required for analysis. A large amount of data from smaller events can be integrated.
2. No hypothesis on the functional form of the scaling laws needs to be formulated before the analysis (Yazd, 1993).
3. Two data sets are computed independently; Fourier velocity spectra and peak filtered velocities. Time and frequency domain amplitudes can be compared simulating peak filtered amplitudes from Fourier spectral velocities, using RVT (Random Vibration Theory).

Observed ground motion is a function of source (Src), site (Site), and path (D(r,f)). Unless non-linear ground motions occur at the site, these three factors are theoretically separable, and additive in terms of logarithms:

$$A(r,f) = Src(r,f) + Site(r,f) + D(r,f) \qquad (3.1)$$

This equation is now modified to emphasize observations. The logarithm of the observed ground motion parameter is a combined effect of site, excitation, and propagation:

$$PEAK = V(r,f) + E(r,f) + D(r,f) \tag{3.2}$$

where r and f are the hypocentral distance and the observed frequency respectively. $E(r,f)$ is the excitation term.

The term excitation is used since the regression only defines the scaling of observed ground motions and says nothing directly about the seismic source. $V(r,f)$ represents the site term. The true separation of those terms is hard due to the trade-offs. We use a piecewise linear function (Anderson and Lei, 1994: Harmsen, 1997) to represent the distance dependence of observed motion, $D(r,f)$, at a fixed frequency, f_c:

$$D(r, f_c) = \sum_{i=1}^{n} L_i(r) D_i \tag{3.3}$$

where $L_i(r)$ is a linear interpretation function and $D_i \equiv D(r_i, f)$ are node values.

We prefer to use a large number of nodes, n, so that the regression can fit any curvature in the actual distance dependence. The ground motion regression model is now written as

$$PEAK = V(r,f) + E(r,f) + \sum_{i=1}^{n} L_i(r) D_i \tag{3.4}$$

The following constraints are used in this study to reduce the number of degrees of freedom of the system to permit a stable inversion:

1. $D(r_{ref}) = 0$, where $r_{ref} = 40$ km. reference distance should be large enough to avoid the effect of source depth error on the hypocentral distance.

2. There is a direct trade-off between a DC offset in all site terms and the excitation.

3. $D(r)$ is smooth. We apply condition $D_{l-1} - 2D_l + D_{l+1} = 0$. This condition is only a linearity constraint if the r_l evenly spaced. For unequally spaced nodes, it ensures a uniform variation in slope between adjacent nodes (Herrmann, 2000).

With these constraints, the regression model can be described in words. We analyze and model both the Fourier velocity and the peak filtered velocity values. Our reason for this extra effort is that this recognizes the imperfections in both the data and the modeling process. The reference distance r_{ref} is selected to be within the range of observed distances so that interpolation is done within the data set rather than extrapolate beyond, to be far enough from the source that errors in source depth do not significantly affect hypocentral distance, and yet not so far that expected super-critically reflected crustal arrivals complicate the motion. For these reasons the reference distance is chosen as 40 km for this study.

3.2 Coda Normalization

Because of concerns about instrument response and unknown source and site effects, we also apply the coda normalization technique (Aki, 1980; Frankel et al., 1990) to provide an estimate of the $D(r,f)$ that should be independent of these unknowns. The coda normalization technique divides the the amplitude of the S or Lg wave amplitude by that of coda wave envelope level. For a linear system, this removes the frequency dependent instrument gain, source excitation, and site amplification effects.

The peak S-wave arrival amplitude, $A_s(r,f)$; and the RMS coda wave level, $A_c(f,t_s)$, at a reference time t_s is used to compute the ratio:

$$A_{reduced}(r,f) = \frac{A_s(r,f)}{A_c(f,t_s)} \tag{3.5}$$

which can be modeled as

$$\log[A_{reduced}(r,f)] = D(r,f) - C(f,t_s) \tag{3.6}$$

where $A_s(r,f)$ is the peak amplitude of the shear wave, and $C(f,t_s)$ is coda envelope. Usually t_s is chosen greater than about twice the direct S wave travel time at which the coda level is independent of the source receiver distance. Through this procedure, the normalized amplitudes yield an initial $D(r,f)$.

4. DATA COLLECTION AND ANALYSIS

4.1 The Eastern Turkey Seismic Experiment (ETSE) Network

Seismic waveform data from a temporary 29-station broadband PASSCAL network were collected in eastern Turkey from late October 1999 to August 2001. The distribution

Turkey

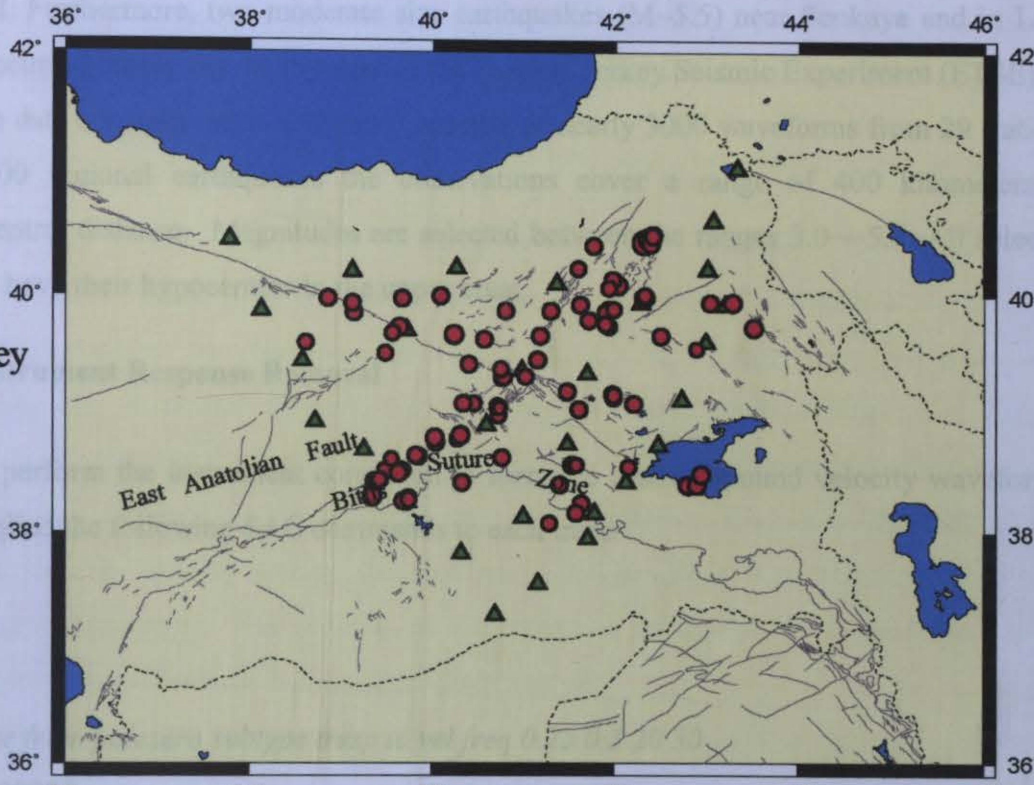

Figure 4.1. Map showing the epicenter and station locations for the Eastern Turkey.

of the seismic stations is such that the network would provide good location of not only any micro-earthquake within the network but also any of the subcrustal earthquakes that are reported to occur in this region and teleseismic events. The network consisted of two main transects: an eastern linear array of twelve stations and a western array of eight stations. The interior of the V shaped array which was formed by the two transects is filled with nine stations spaced approximately 100 km apart (Figure 4.1). Each broadband station was equipped with a Streckeisen STS-2 seismometer, except for station EZRM. A Guralp

CMG-3T seismometer was used at EZRM. 24 bit broadband data continuously recorded at 4 sps (sample per second), which was high enough for accurate event locations. The hypocentral locations and the crustal model were tested and calibrated by a 12-ton controlled source explosion that took place in Eastern Turkey on June 5, 2001 (Gurbuz et al., 2003). All hypocenter locations were classified into four different categories based on the reliability of the locations (Class A, B, C, and D). During the experiment, approximately 10 events per day were detected and a total of 1165 local earthquakes were located. Furthermore, two moderate size earthquakes (M~5.5) near Senkaya and in Lake Van occurred during the deployment of the Eastern Turkey Seismic Experiment (ETSE).

The data set analyzed in this paper consists of nearly 3000 waveforms from 29 stations and 100 regional earthquakes the observations cover a range of 400 kilometers in hypocentral distance. Magnitudes are selected between the ranges 3.0 – 5.5. All selected events have their hypocenters in the upper crust.

4.2 Instrument Response Removal

To perform the instrument correction to form the desired ground velocity waveforms, we applied the following SAC commands to each trace:

rtr
taper
transfer from polezero subtype tresp to vel freq 0.25 0.3 20 30
div 1000000

Here we remove the linear trend in the data set, taper the beginning and end of the time series, remove the instrument response given by the file tresp after bandpass filtering the data between 0.3 - 20 Hz. Then it is converted to units of meter/sec by dividing by factor 1000000. The bandpass filter used within the transfer command is required to ensure stability of the deconvolution process. The band limits are chosen so that they do not interfere with the bandpass filtering to be performed in the next step of processing. Careful correction for instrument response is critical to this study since we will attempt to study the absolute scaling of ground motion generated by the source.

4.3 Trace Analysis

Digital waveforms are acquired from the ETSE network. Each trace is previewed to remove clipped ones or otherwise bad waveforms. For each waveform, the arrival times of P and S waves were picked for two reasons. First to provide a quick check on the event location by using the difference in P- and S-wave arrival times to estimate the epicentral distance. The other reason is that an analysis of peak S-wave motion requires knowledge of where the S wave actually begins.

To study the frequency dependence of ground motion, each waveform was filtered about a center frequency, f_c, by an 8-pole high pass causal Butterworth filter with corner frequency at $(\frac{f_c}{\sqrt{2}})$ Hz, followed by an 8-pole low pass Butterworth filter with corner frequency at $\sqrt{2}f_c$ Hz. The center frequencies used were 0.3, 0.5, 0.7, 1, 2, 3, 4, 6, 8 and 10 Hz. The peak filtered ground velocity was saved. In addition a duration window was defined in terms of the 5% and 75% bounds of the normalized integral signal-squared following the S arrival (Figure 4.3) The signal within this window was Fourier transformed, and a smoothed estimate of the Fourier velocity spectra was made between the two filter corners for each center frequency. For each filter frequency, the peak filtered motion, Fourier velocity spectra, duration and signal envelope were tabulated for use in later processing steps. The purpose of the extensive tabulation is to preserve enough information to characterize the signal for later analysis.

The source-receiver distance distribution for the whole dataset is shown in Figure 4.2 The y-axis of the plot displays the station names, and the x-axis shows the source-receiver hypocentral distance. In practice plotting the observation distances by event and by station is a good diagnostic for discarding event or for defining the distance nodes. The goal is that each station observes events over a wide range of distances overlapping those of other stations, and that the distance ranges of events overlap. The Data set used in this study has good overlapping distance sampling by stations which is required for stable inversion.

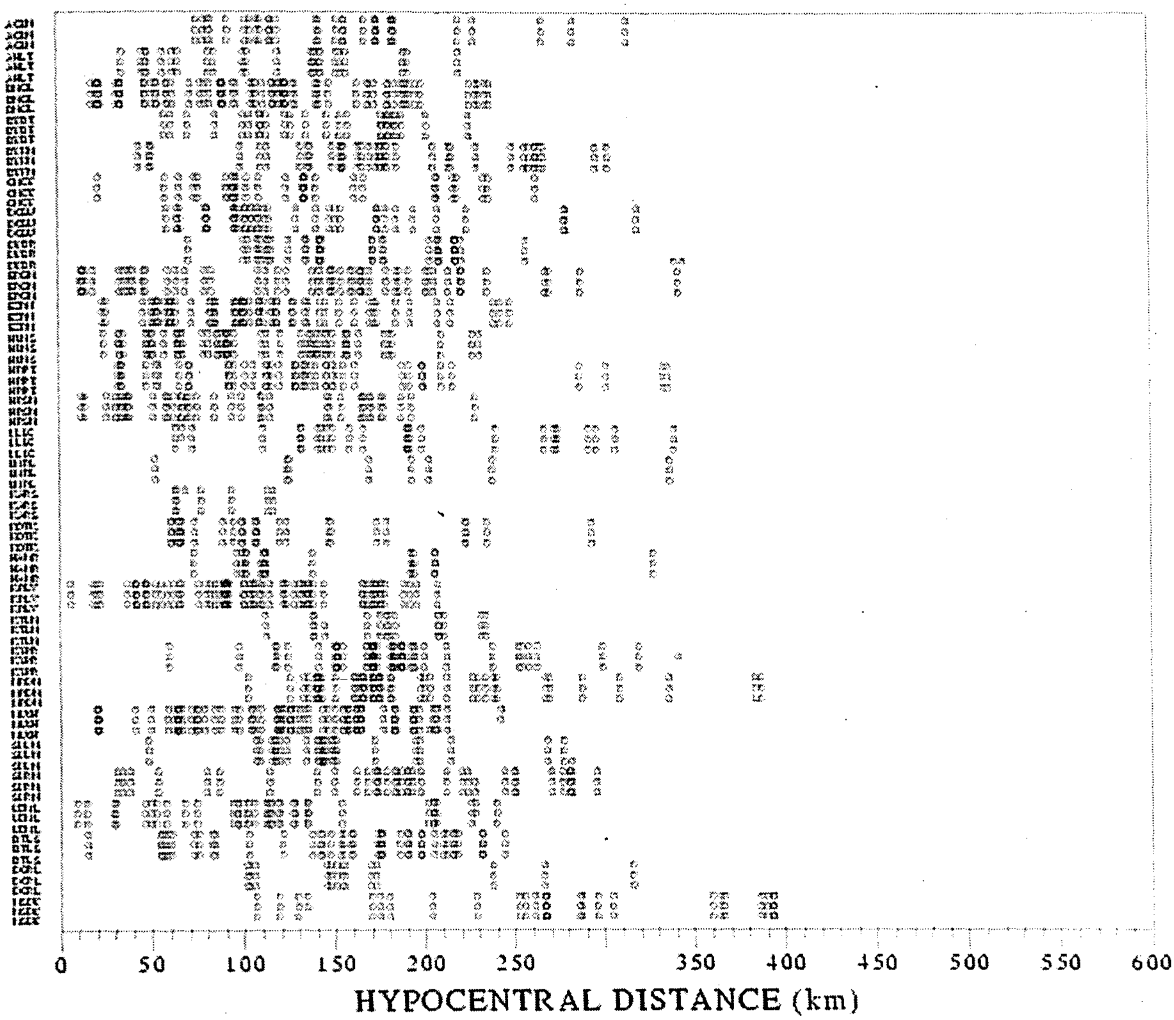

Figure 4.2. Source-receiver hypocentral distance distribution of observed station for the data recorded along the seismic network

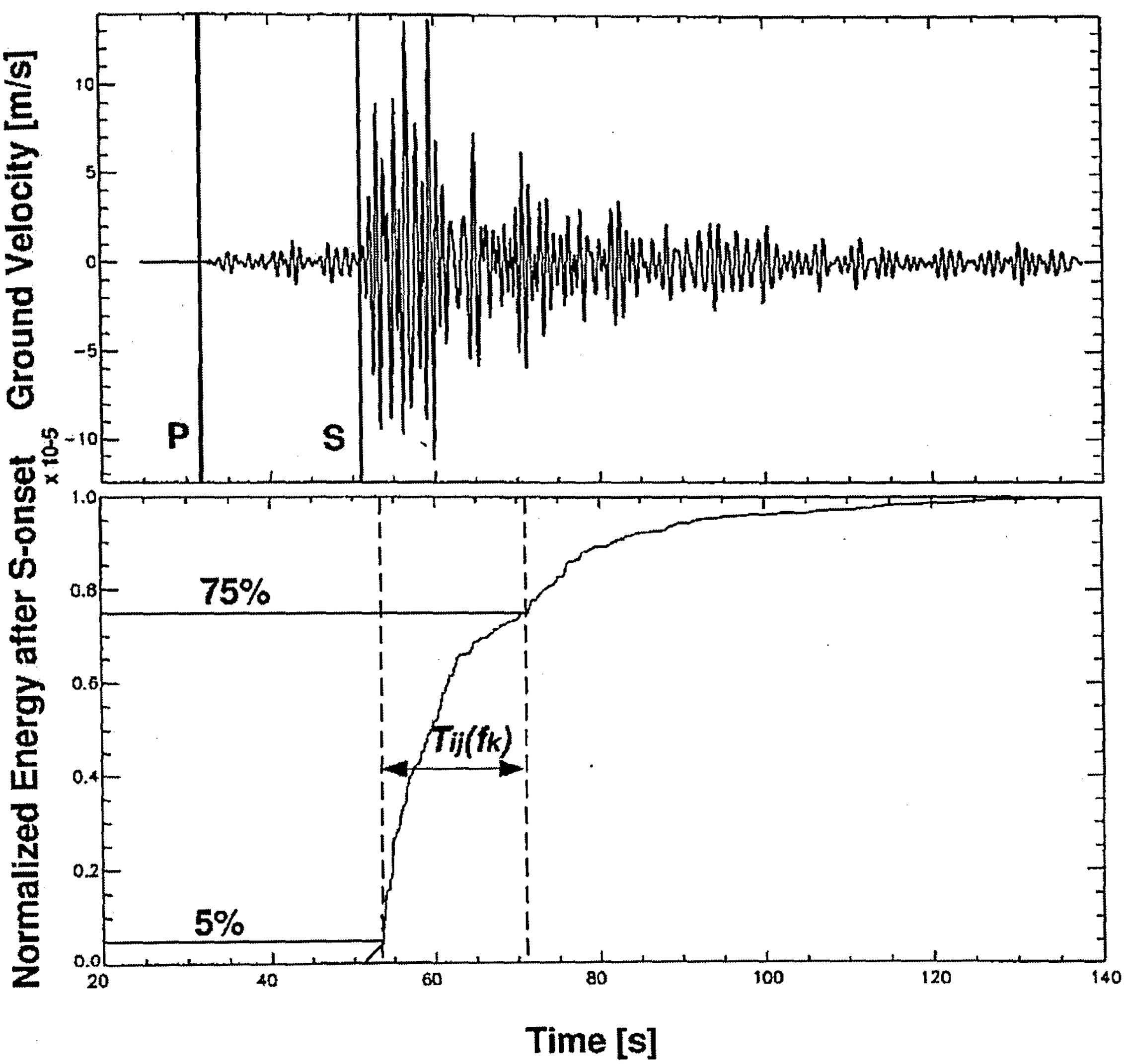

Figure 4.3. Illustration of the method used to determine the duration. The upper trace is the velocity time history peak filtered at 1 Hz. The *P*- and *S*-arrival times of the unfiltered time series are plotted. The lower trace is the integrated square velocity. The energy (the integrated square velocity) following the onset of the *S* waves is normalized to the level of the plateau. The time window for which 5%–75% of energy is reached is computed. This time window is defined as $T_{ij}(f_k)$ of the specific seismogram at f_k=1 Hz. [Bay et al., 2003]

5. GENERAL DATA REGRESSION AND MODELING

5.1 Regression

5.1.1 Regression of Fourier Velocity Spectra

For regression analysis velocity spectra of waveforms were calculated. This calculation was done for certain frequency band. Selection of frequency band is done from the spectral content of the data. Figures 5.1, 5.2, 5.3, and 5.4 give typical examples of the regression analysis at filter frequencies of 0.3, 1.0, 4.0 and 10.0 Hz on the Fourier velocity spectra data set. It also shows the initial propagation term estimated by the coda normalization technique. The initial and final propagation functionals show good agreement for the Fourier velocity spectra data set except at 10 Hz. This may be due to lack of observations. The regression residual plot shows that the distance nodes were appropriate to determine D(r).

Figure 5.5 shows distance scaling of the D(r) term at the ten different frequencies for regression on the Fourier velocity spectra. This figure is corrected for an r^{-1} (geometrical spreding) trend to emphasize departure (scattering, deviation) of high frequency spectra with distance from r^{-1} spreading. As expected the 10 Hz signal decreases more rapidly with distance than lower frequencies.

Table 5.1, Table 5.2, and Table 5.3 give the numerical results of our regression on the regional attenuation functional of Fourier Velocity spectra for eastern Turkey. They give the corroesponding value D(r) for each frequency and distance as well as the number of observations available at the specific distance.

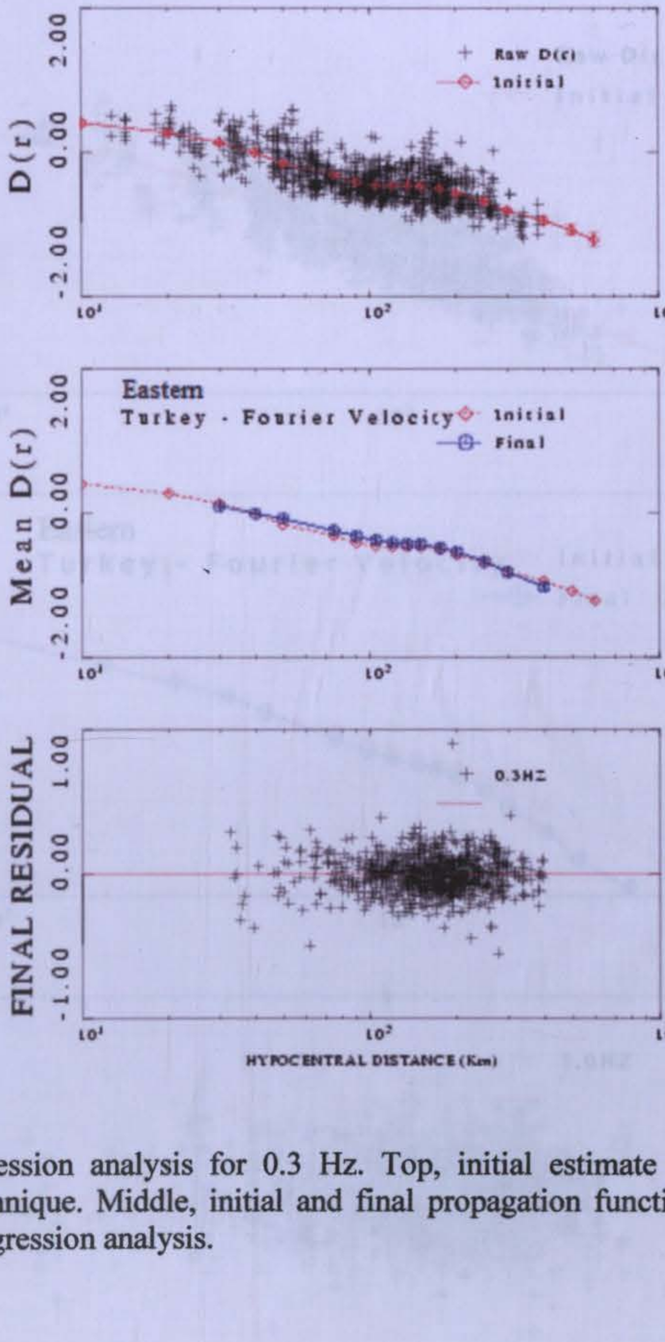

Figure 5.1. Regression analysis for 0.3 Hz. Top, initial estimate of D(r) using coda normalization technique. Middle, initial and final propagation functionals. Bottom, final residuals of the regression analysis.

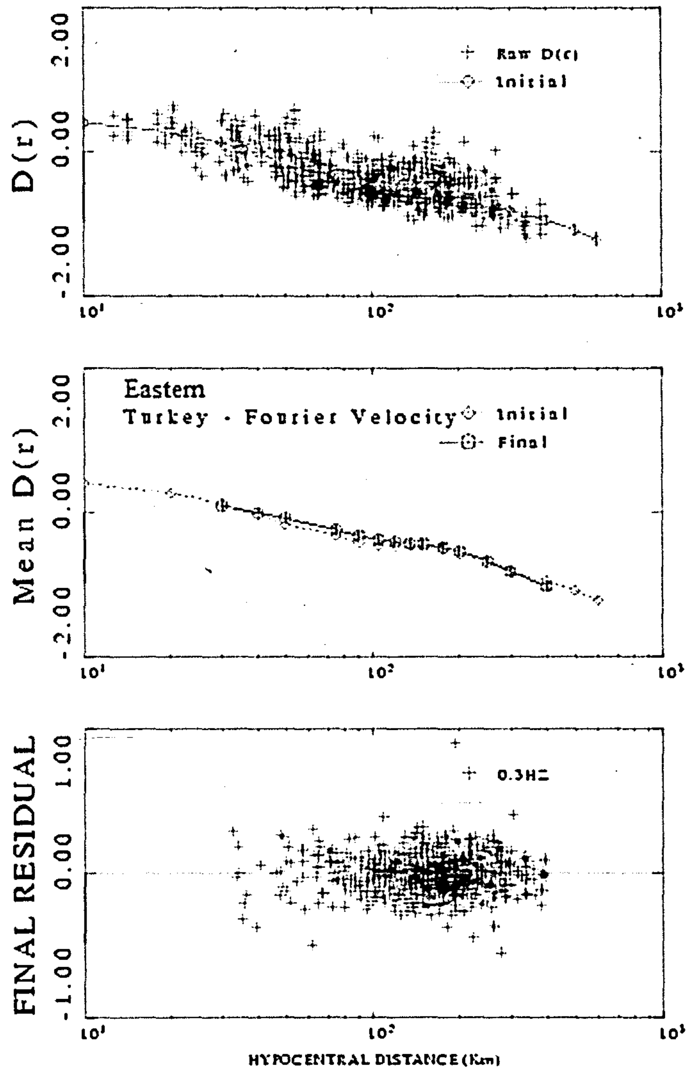

Figure 5.1. Regression analysis for 0.3 Hz. Top, initial estimate of D(r) using coda normalization technique. Middle, initial and final propagation functionals. Bottom, final residuals of the regression analysis.

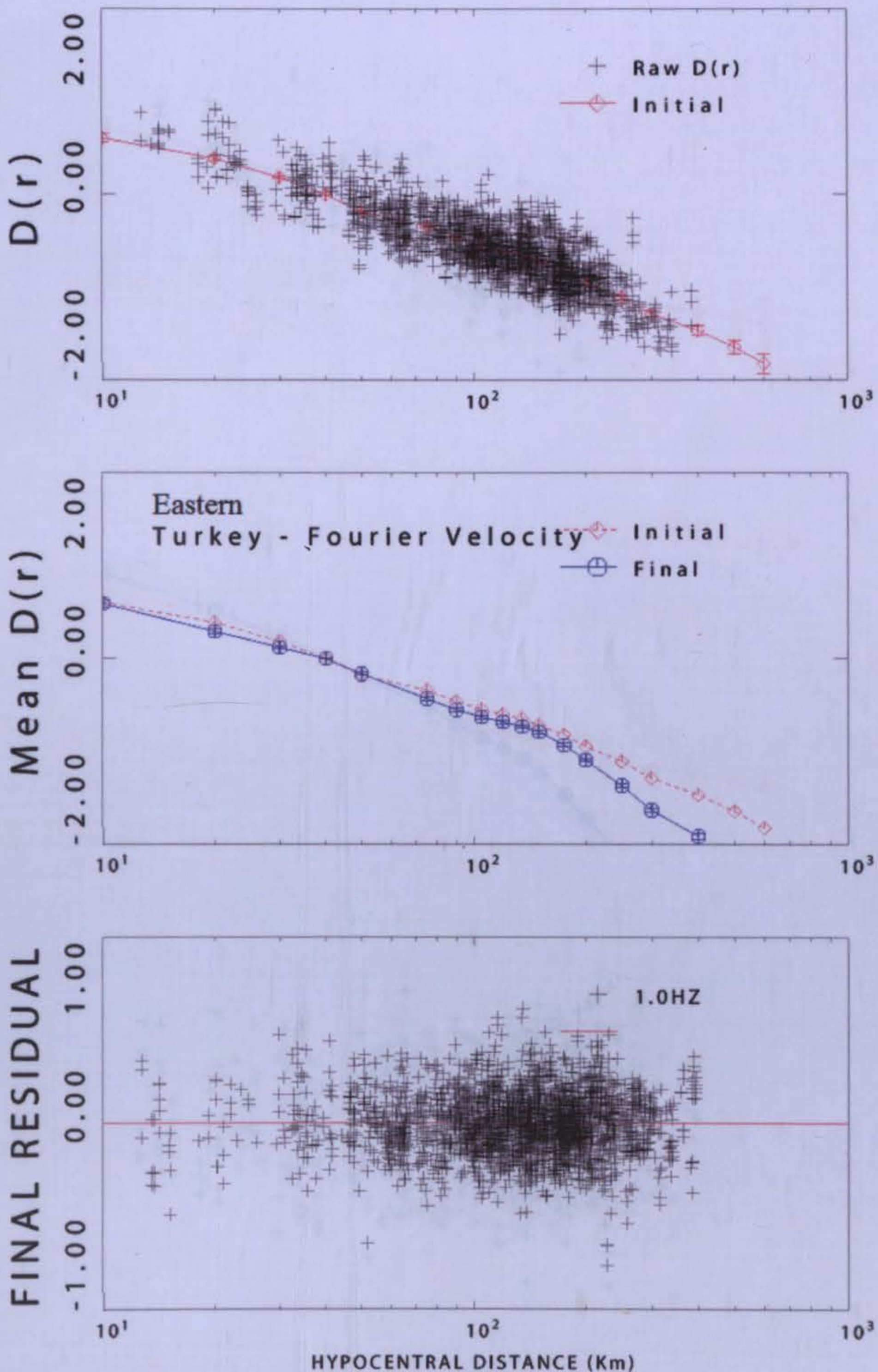

Figure 5.2. Regression analysis for 1.0 Hz. Top, initial estimate of D(r) using coda normalization technique. Middle, initial and final propagation functionals. Bottom, final residuals of the regression analysis.

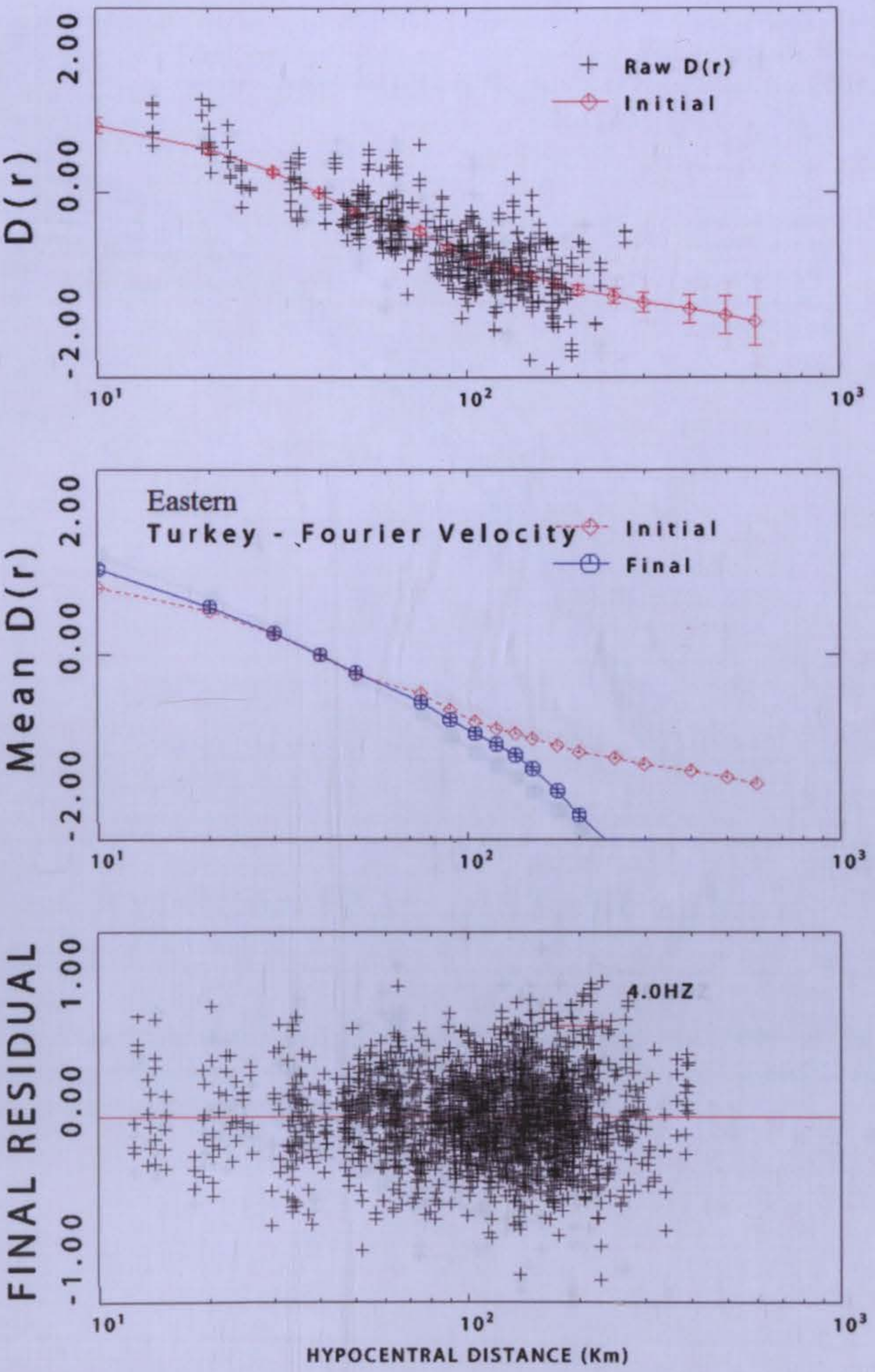

Figure 5.3. Regression analysis for 4.0 Hz. Top, initial estimate of D(r) using coda normalization technique. Middle, initial and final propagation functionals. Bottom, final residuals of the regression analysis.

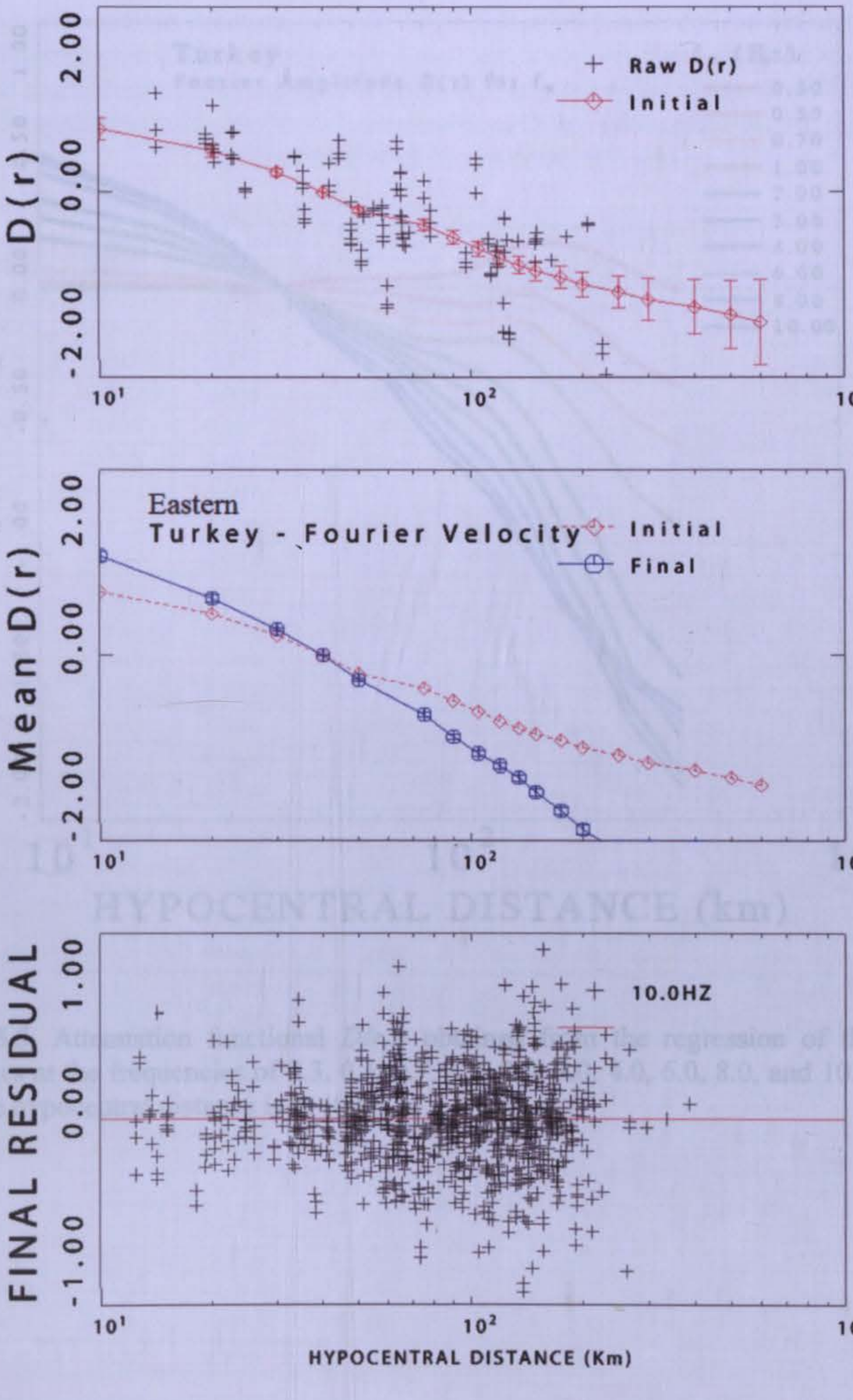

Figure 5.4. Regression analysis for 10.0 Hz. Top, initial estimate of D(r) using coda normalization technique. Middle, initial and final propagation functionals. Bottom, final residuals of the regression analysis.

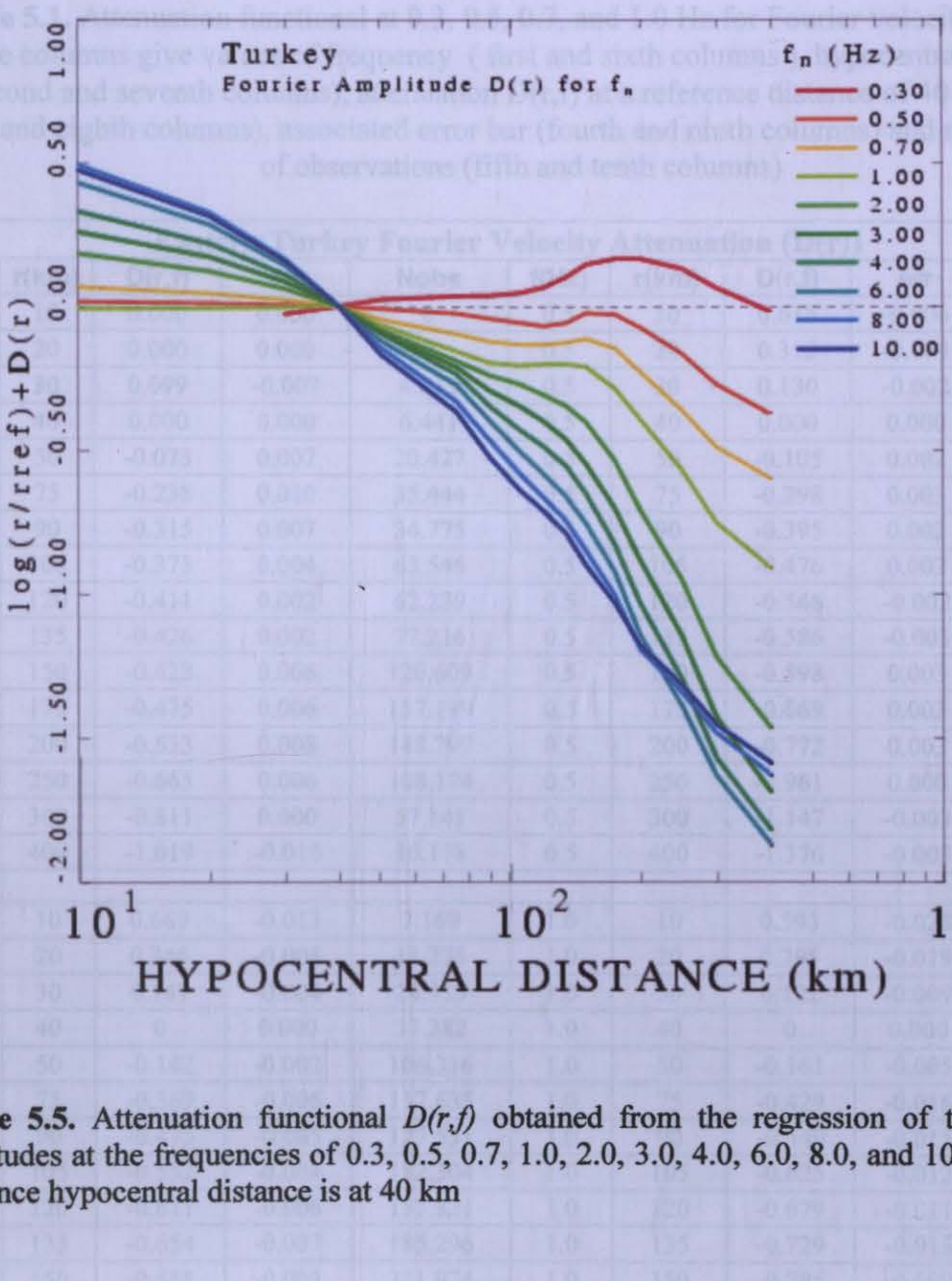

Figure 5.5. Attenuation functional *D(r,f)* obtained from the regression of the Fourier amplitudes at the frequencies of 0.3, 0.5, 0.7, 1.0, 2.0, 3.0, 4.0, 6.0, 8.0, and 10.0 Hz. The reference hypocentral distance is at 40 km

Table 5.1. Attenuation functional at 0.3, 0.5, 0.7, and 1.0 Hz for Fourier velocity spectra. The columns give values of frequency (first and sixth columns), hypocentral distance second and seventh columns), attenuation D(r,f) at a reference distance of 40 km (third and eighth columns), associated error bar (fourth and ninth columns) and number of observations (fifth and tenth columns)

Eastern Turkey Fourier Velocity Attenuation (D(r))									
F(Hz)	r(km)	D(r,f)	err	Nobs	f(Hz)	r(km)	D(r,f)	err	Nobs
0.3	10	0.000	0.000	0	0.5	10	0.618	-0.006	3.67
0.3	20	0.000	0.000	0	0.5	20	0.312	-0.004	4.965
0.3	30	0.099	-0.007	4.813	0.5	30	0.130	-0.002	11.925
0.3	40	0.000	0.000	6.441	0.5	40	0.000	0.000	20.956
0.3	50	-0.073	0.007	20.427	0.5	50	-0.105	0.002	58.472
0.3	75	-0.238	0.010	35.444	0.5	75	-0.298	0.003	69.011
0.3	90	-0.315	0.007	34.775	0.5	90	-0.395	0.002	81.947
0.3	105	-0.373	0.004	63.546	0.5	105	-0.476	0.002	127.228
0.3	120	-0.411	0.002	62.239	0.5	120	-0.546	-0.002	128.799
0.3	135	-0.426	0.002	77.216	0.5	135	-0.586	-0.003	139.591
0.3	150	-0.428	0.006	120.609	0.5	150	-0.598	0.003	189.366
0.3	175	-0.475	0.006	157.199	0.5	175	-0.669	0.003	239.47
0.3	200	-0.533	0.008	148.797	0.5	200	-0.772	0.003	209.786
0.3	250	-0.665	0.006	108.174	0.5	250	-0.961	0.000	143.088
0.3	300	-0.811	0.000	57.141	0.5	300	-1.147	-0.003	76.501
0.3	400	-1.019	-0.010	16.178	0.5	400	-1.376	-0.003	21.225
0.7	10	0.669	-0.013	7.169	1.0	10	0.593	-0.028	11.664
0.7	20	0.346	-0.008	13.275	1.0	20	0.295	-0.019	23.036
0.7	30	0.147	-0.004	24.935	1.0	30	0.122	-0.009	32.213
0.7	40	0	0.000	37.282	1.0	40	0	0.000	40.789
0.7	50	-0.142	-0.002	106.316	1.0	50	-0.161	-0.005	129.083
0.7	75	-0.369	-0.006	117.635	1.0	75	-0.429	-0.016	155.585
0.7	90	-0.475	-0.005	127.531	1.0	90	-0.549	-0.015	150.054
0.7	105	-0.552	-0.004	182.304	1.0	105	-0.625	-0.012	211.137
0.7	120	-0.611	-0.006	157.321	1.0	120	-0.679	-0.011	190.184
0.7	135	-0.654	-0.007	185.296	1.0	135	-0.729	-0.013	202.606
0.7	150	-0.688	-0.003	231.974	1.0	150	-0.785	-0.009	258.35
0.7	175	-0.787	-0.003	283.506	1.0	175	-0.927	-0.013	328.339
0.7	200	-0.926	-0.003	255.577	1.0	200	-1.091	-0.008	286.319
0.7	250	-1.158	-0.008	153.45	1.0	250	-1.366	-0.014	181.26
0.7	300	-1.365	-0.007	83.481	1.0	300	-1.629	-0.015	95.154
0.7	400	-1.6	0.000	21.949	1.0	400	-1.911	-0.007	29.227

Table 5.2. Attenuation functional at 2.0, 3.0, 4.0, and 6.0 Hz for Fourier Velocity spectra. The columns give values of frequency (first and sixth columns), hypocentral distance (second and seventh columns), attenuation D(r,f) at a reference distance of 40 km (third and eighth columns), associated error bar (fourth and ninth columns) and number of observations (fifth and tenth columns).

Eastern Turkey Fourier Velocity Attenuation (D(r))									
f(Hz)	r(km)	D(r,f)	err	Nobs	f(Hz)	r(km)	D(r,f)	err	Nobs
2.0	10	0.785	-0.009	14.412	3.0	10	0.860	-0.003	15.041
2.0	20	0.423	-0.006	29.655	3.0	20	0.473	-0.002	39.43
2.0	30	0.186	-0.003	45.439	3.0	30	0.211	-0.001	50.661
2.0	40	0.000	0.000	55.184	3.0	40	0.000	0.000	63.29
2.0	50	-0.177	0.001	167.584	3.0	50	-0.187	0.004	176.924
2.0	75	-0.463	-0.009	188.373	3.0	75	-0.484	-0.003	186.712
2.0	90	-0.593	-0.005	159.608	3.0	90	-0.646	-0.003	162.975
2.0	105	-0.689	-0.002	219.131	3.0	105	-0.765	0.000	212.803
2.0	120	-0.786	-0.005	191.746	3.0	120	-0.878	-0.001	181.533
2.0	135	-0.875	-0.005	206.871	3.0	135	-0.992	-0.002	196.273
2.0	150	-0.978	-0.002	261.449	3.0	150	-1.123	0.001	225.772
2.0	175	-1.178	-0.005	320.027	3.0	175	-1.345	-0.003	285.709
2.0	200	-1.407	-0.001	266.463	3.0	200	-1.582	0.004	216.367
2.0	250	-1.750	-0.005	157.393	3.0	250	-1.946	-0.003	115.875
2.0	300	-2.097	-0.008	83.468	3.0	300	-2.307	-0.007	58.543
2.0	400	-2.468	-0.004	23.196	3.0	400	-2.690	-0.003	18.093
4.0	10	0.931	0.004	14.622	6.0	10	1.030	0.007	13.623
4.0	20	0.520	0.003	37.315	6.0	20	0.586	0.005	38.293
4.0	30	0.235	0.001	48.744	6.0	30	0.268	0.002	51.57
4.0	40	0.000	0.000	57.378	6.0	40	0.000	0.000	58.458
4.0	50	-0.190	0.009	175.097	6.0	50	-0.215	0.008	172.165
4.0	75	-0.508	0.002	185.434	6.0	75	-0.546	0.003	177.491
4.0	90	-0.700	0.001	160.392	6.0	90	-0.751	0.003	143.861
4.0	105	-0.847	0.002	206.947	6.0	105	-0.921	0.002	176.124
4.0	120	-0.966	0.003	176.725	6.0	120	-1.062	0.002	161.475
4.0	135	-1.084	0.004	191.091	6.0	135	-1.191	0.003	156.021
4.0	150	-1.227	0.007	215.904	6.0	150	-1.331	0.009	173.841
4.0	175	-1.471	0.002	256.434	6.0	175	-1.566	0.007	176.145
4.0	200	-1.732	0.006	176.978	6.0	200	-1.844	0.003	109.208
4.0	250	-2.096	0.000	78.462	6.0	250	-2.189	-0.003	39.664
4.0	300	-2.448	-0.003	35.968	6.0	300	-2.510	-0.005	14.308
4.0	400	-2.822	0.002	15.51	6.0	400	-2.873	-0.006	5.753

Table 5.3. Attenuation functional at 8.0 and 10.0 Hz for Fourier Velocity spectra. The columns give values of frequency (first and sixth columns), hypocentral distance (second and seventh columns), attenuation D(r,f) at a reference distance of 40 km (third and eighth columns), associated error bar (fourth and ninth columns) and number of observations (fifth and tenth columns).

Eastern Turkey Fourier Velocity Attenuation (D(r))									
f(Hz)	r(km)	D(r,f)	err	Nobs	F(Hz)	r(km)	D(r,f)	err	Nobs
8.0	10	1.093	0.006	14.743	10.0	10	1.075	-0.005	13.388
8.0	20	0.628	0.004	34.505	10.0	20	0.616	-0.003	37.456
8.0	30	0.289	0.002	51.307	10.0	30	0.283	-0.002	48.015
8.0	40	0.000	0.000	59.724	10.0	40	0.000	0.000	51.996
8.0	50	-0.239	0.009	163.423	10.0	50	-0.262	0.004	144.929
8.0	75	-0.603	0.000	164.73	10.0	75	-0.639	-0.004	143.896
8.0	90	-0.819	0.001	126.313	10.0	90	-0.878	-0.007	103.906
8.0	105	-0.998	0.001	148.269	10.0	105	-1.056	-0.005	101.921
8.0	120	-1.144	0.002	130.457	10.0	120	-1.190	0.000	88.096
8.0	135	-1.275	0.006	117.766	10.0	135	-1.319	0.004	89.752
8.0	150	-1.425	0.008	135.633	10.0	150	-1.476	0.002	89.765
8.0	175	-1.648	0.004	118.372	10.0	175	-1.674	-0.002	71.308
8.0	200	-1.892	-0.005	56.405	10.0	200	-1.878	-0.007	31.409
8.0	250	-2.140	-0.001	17.139	10.0	250	-2.115	-0.009	9.02
8.0	300	-2.360	0.006	2.353	10.0	300	-2.331	-0.010	2.919
8.0	400	-2.630	0.011	3.859	10.0	400	-2.589	-0.011	1.225

5.1.2 Regression of Peak Filtered Velocity

Figures 5.6, 5.7, 5.8, and 5.9 give examples of the regression analysis for the band pass filtered spectra data set at 0.3, 1.0, 4.0, and 10.0 Hz. It also shows the initial propagation term estimated from the coda normalization technique. The initial and final propagation functional shows good agreement for the band pass filtered spectra data set except 10 Hz. The regression residual plot is used to see if the distance nodes were appropriate to determine D(r). Fourier velocity spectra residuals show slightly less scatter than band-pass filtered residuals and residuals of two data sets increase at higher frequencies. Residual values are high at a distance of 135 km for both data sets. Figure 4.5 shows the vertical component distance scaling of the peak filtered velocity D(r) term at ten different frequencies for Eastern Turkey. This D(r) values are corrected for an r^{-1} trend to emphasize departure from simple r^{-1} spreading. (Fig 5.10)

Table 5.4, 5.5, and Table 5.6 give the numerical results of our regression on the regional attenuation functional for the eastern Turkey. They give the corresponding value of D(r) for each frequency and distance as well as the number of observations contributing to each node.

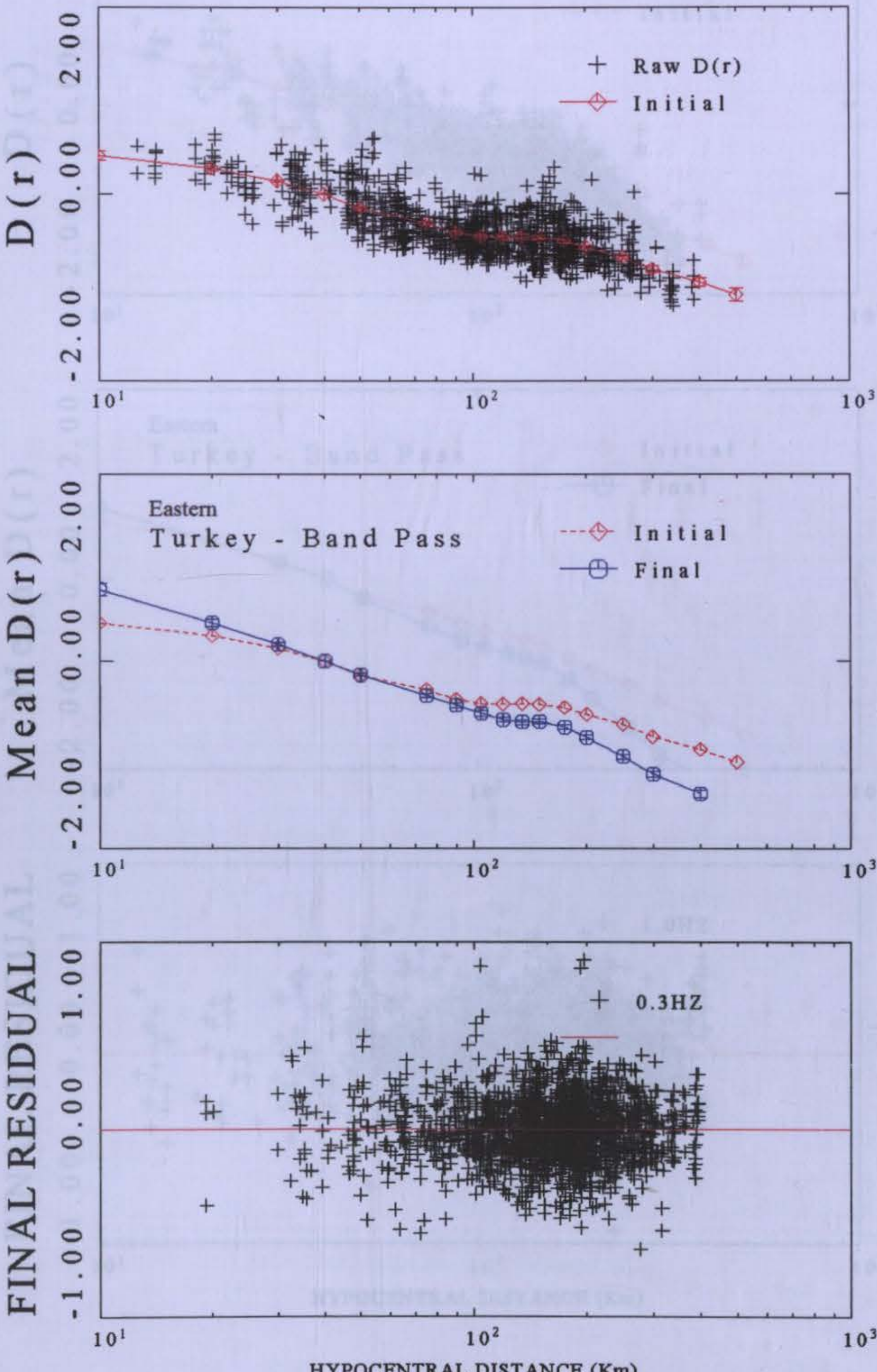

Figure 5.6. Regression analysis for 0.3 Hz. Top, initial estimate of D(r) using coda normalization technique. Middle, initial and final propagation functionals. Bottom, final residuals of the regression analysis.

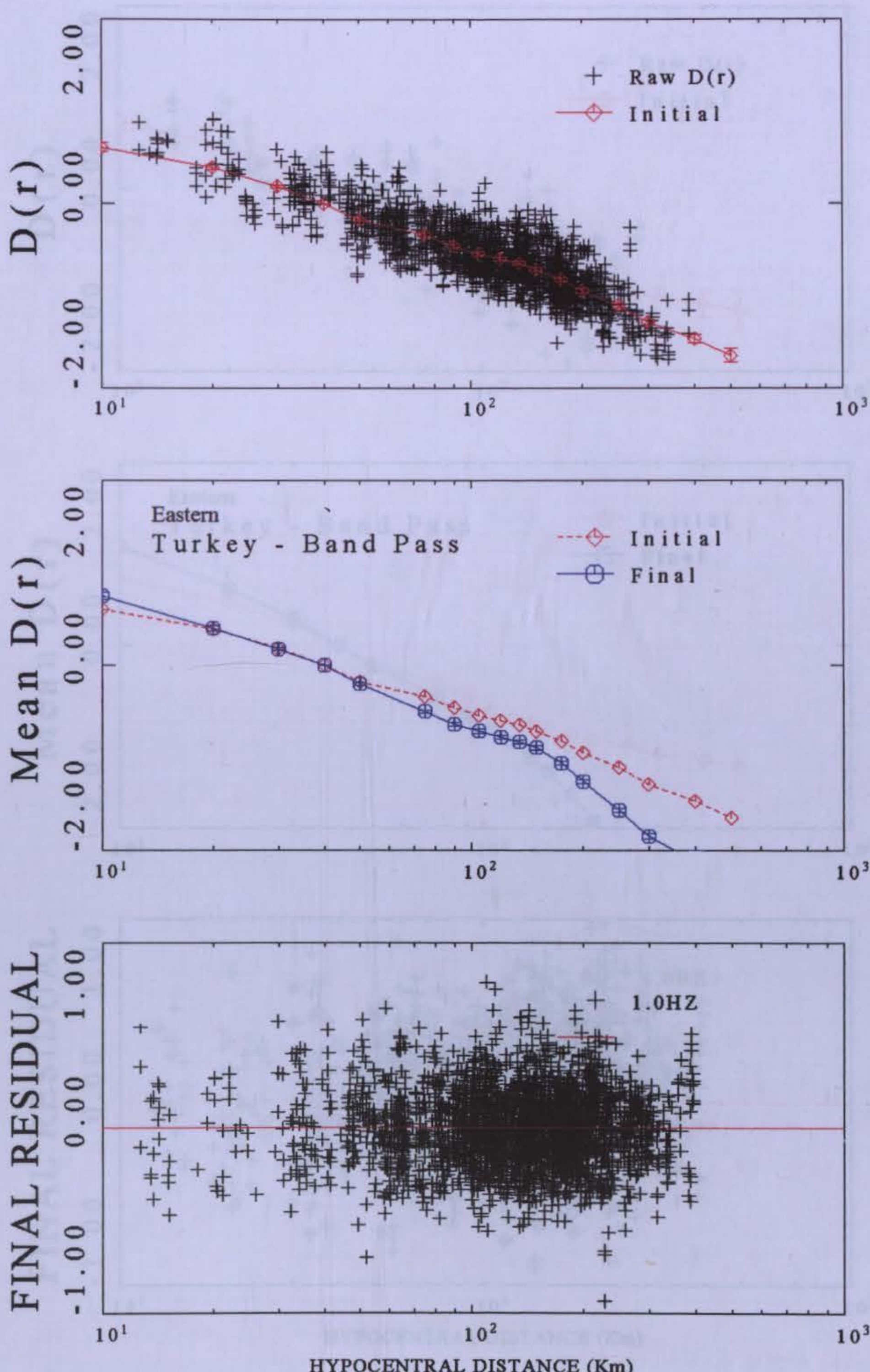

Figure 5.7. Regression analysis for 1.0 Hz. Top, initial estimate of D(r) using coda normalization technique. Middle, initial and final propagation functionals. Bottom, final residuals of the regression analysis.

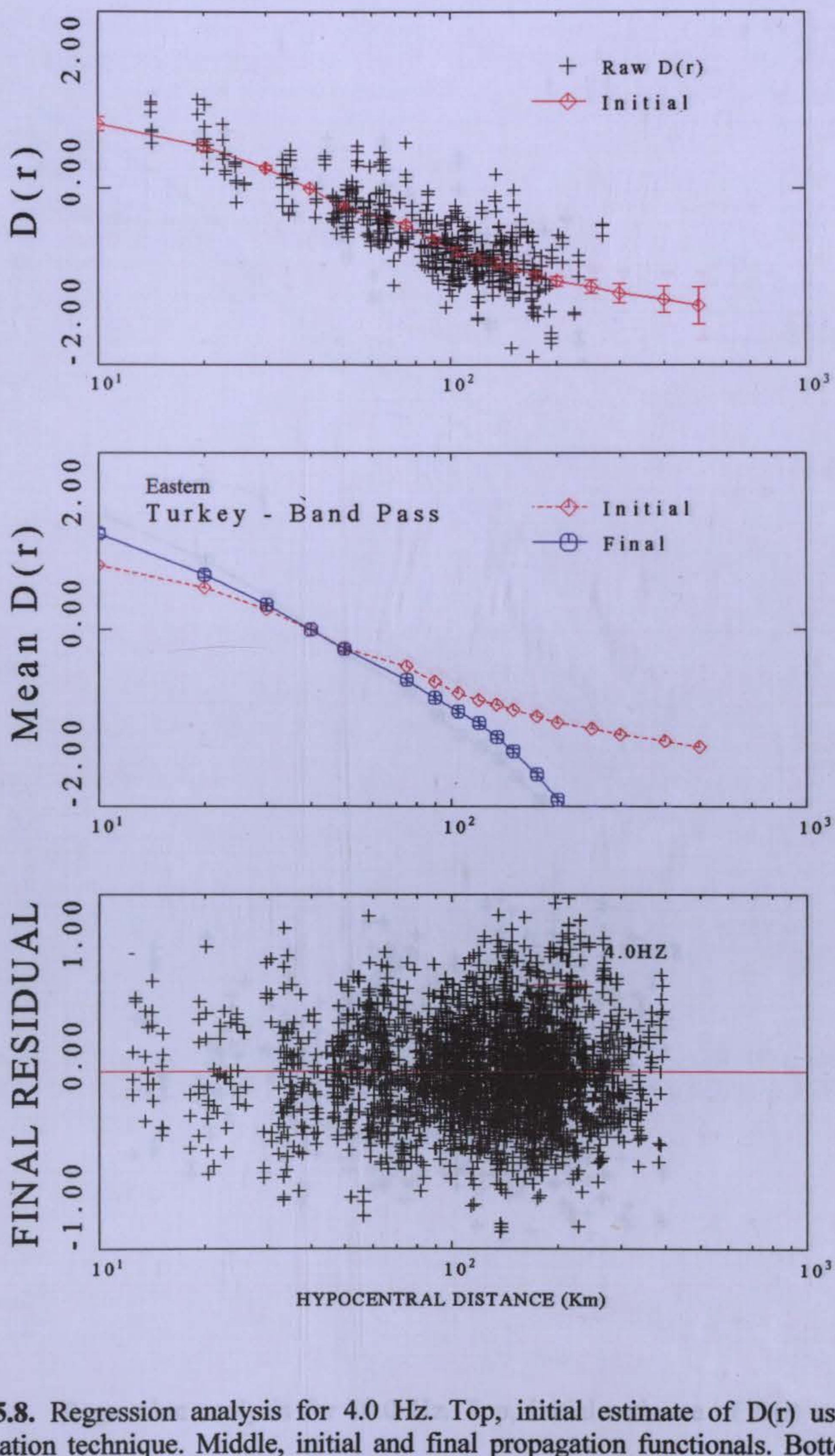

Figure 5.8. Regression analysis for 4.0 Hz. Top, initial estimate of D(r) using coda normalization technique. Middle, initial and final propagation functionals. Bottom, final residuals of the regression analysis.

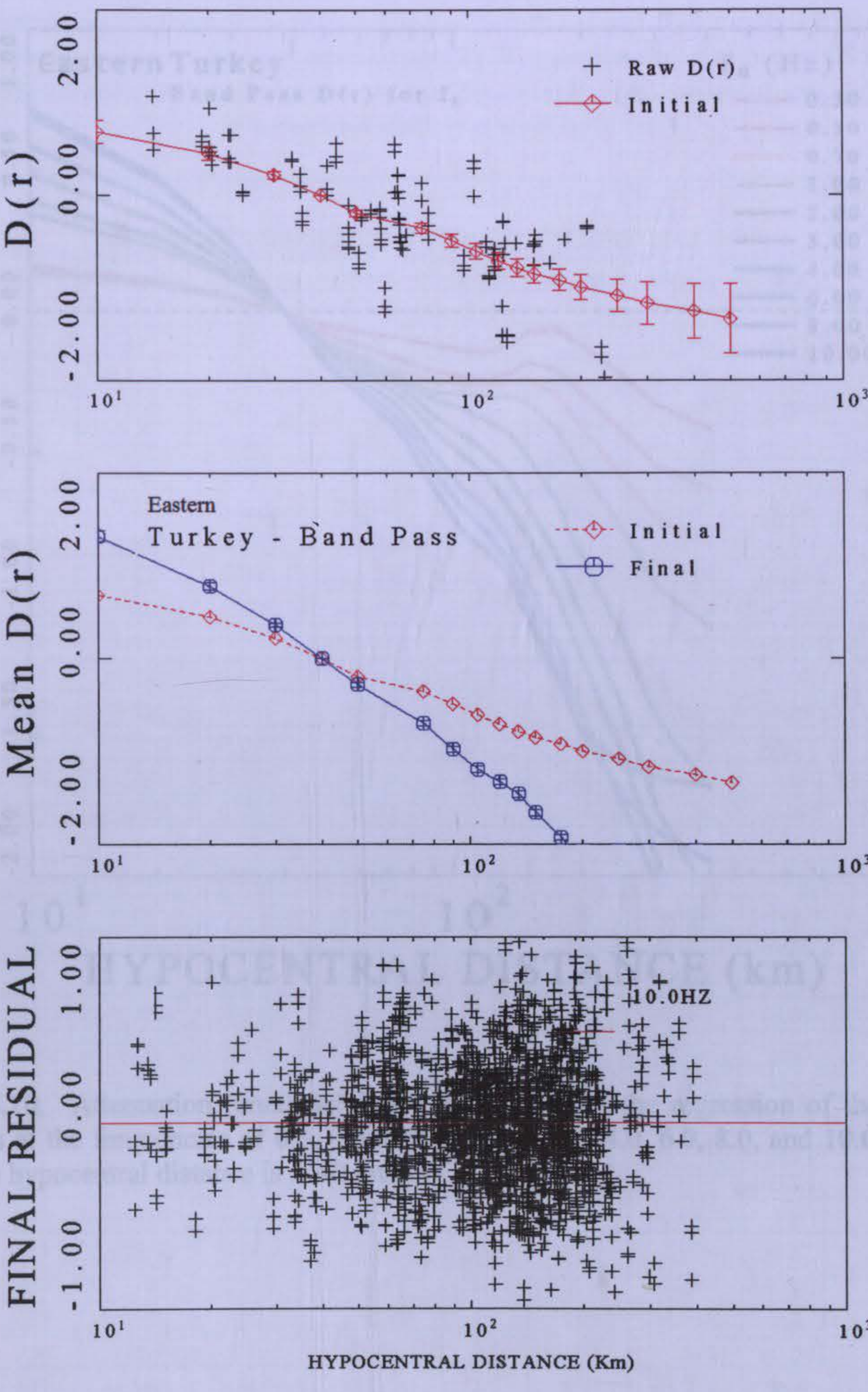

Figure 5.9. Regression analysis for 10.0 Hz. Top, initial estimate of D(r) using coda normalization technique. Middle, initial and final propagation functionals. Bottom, final residuals of the regression analysis.

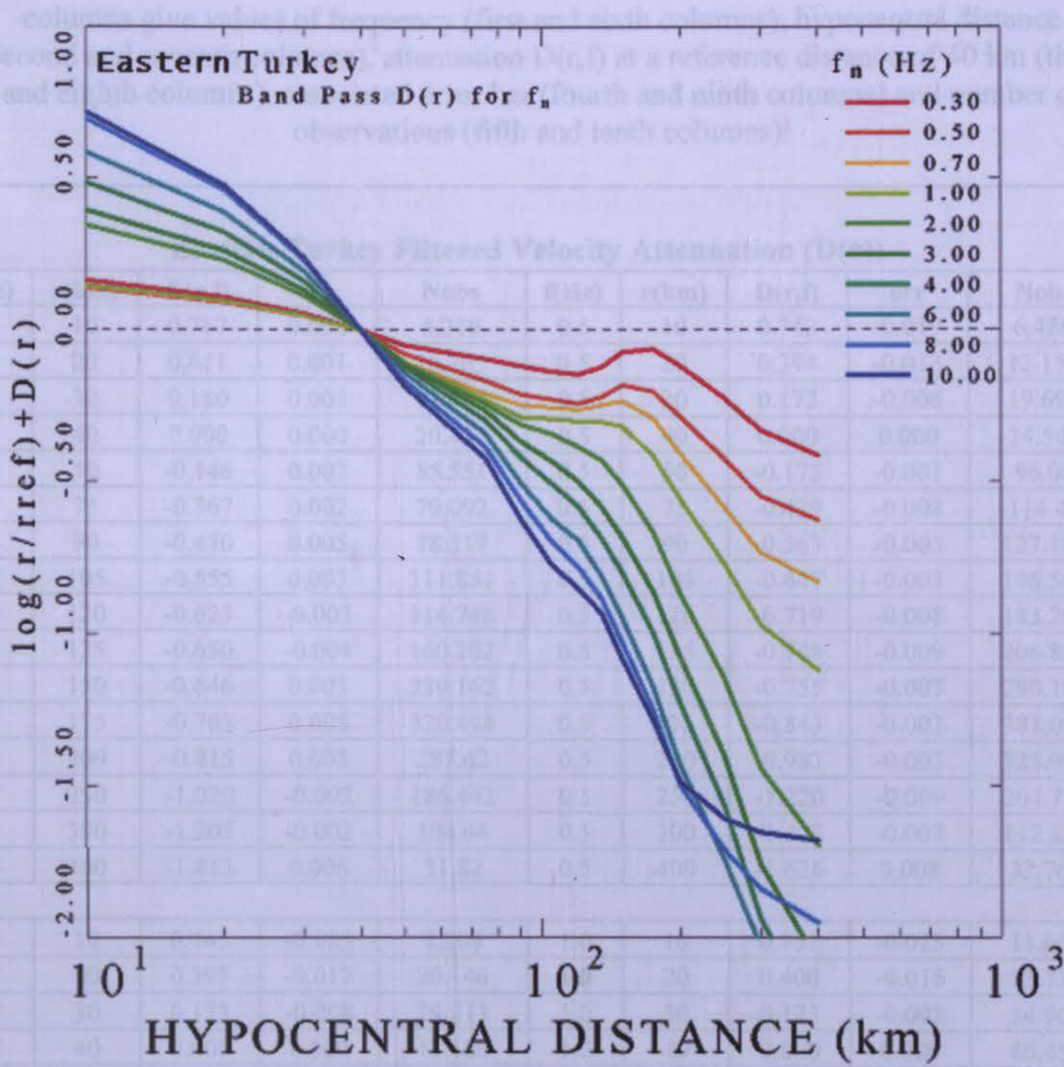

Figure 5.10. Attenuation functional *D(r,f)* obtained from the regression of the Filtered velocities at the frequencies of 0.3, 0.5, 0.7, 1.0, 2.0, 3.0, 4.0, 6.0, 8.0, and 10.0 Hz. The reference hypocentral distance is at 40 km.

Table 5.4. Attenuation functional at 0.3, 0.7, 1.0, and 2.0 Hz for Band-Pass filtered. The columns give values of frequency (first and sixth columns), hypocentral distance (second and seventh columns), attenuation D(r,f) at a reference distance of 40 km (third and eighth columns), associated error bar (fourth and ninth columns) and number of observations (fifth and tenth columns).

Eastern Turkey Filtered Velocity Attenuation (D(r))									
f(Hz)	**r(km)**	**D(r,f)**	**err**	**Nobs**	**f(Hz)**	**r(km)**	**D(r,f)**	**err**	**Nobs**
0.3	10	0.767	0.002	5.219	0.5	10	0.742	-0.019	6.486
0.3	20	0.411	0.001	10.765	0.5	20	0.394	-0.013	12.157
0.3	30	0.180	0.001	12.443	0.5	30	0.172	-0.006	19.691
0.3	40	0.000	0.000	20.434	0.5	40	0.000	0.000	34.506
0.3	50	-0.146	0.002	55.551	0.5	50	-0.175	-0.001	96.08
0.3	75	-0.367	0.002	79.092	0.5	75	-0.439	-0.008	114.45
0.3	90	-0.470	0.005	78.517	0.5	90	-0.563	-0.005	127.187
0.3	105	-0.555	0.003	111.851	0.5	105	-0.647	-0.003	196.505
0.3	120	-0.623	-0.003	114.748	0.5	120	-0.719	-0.008	183.294
0.3	135	-0.650	-0.004	160.202	0.5	135	-0.748	-0.009	206.832
0.3	150	-0.646	0.003	239.162	0.5	150	-0.755	-0.003	290.105
0.3	175	-0.703	0.005	320.494	0.5	175	-0.843	-0.003	381.099
0.3	200	-0.815	0.003	287.62	0.5	200	-0.983	-0.003	325.999
0.3	250	-1.020	-0.002	186.442	0.5	250	-1.220	-0.009	204.717
0.3	300	-1.205	-0.002	104.64	0.5	300	-1.422	-0.007	112.124
0.3	400	-1.413	0.006	31.82	0.5	400	-1.626	0.008	32.768

0.7	10	0.745	-0.025	7.208	1.0	10	0.751	-0.023	11.664
0.7	20	0.397	-0.017	20.146	1.0	20	0.400	-0.016	23.732
0.7	30	0.173	-0.008	29.813	1.0	30	0.175	-0.008	34.904
0.7	40	0.000	0.000	43.186	1.0	40	0.000	0.000	46.451
0.7	50	-0.201	-0.006	136.863	1.0	50	-0.201	-0.004	155.897
0.7	75	-0.482	-0.015	155.96	1.0	75	-0.502	-0.015	184.05
0.7	90	-0.598	-0.010	158.308	1.0	90	-0.639	-0.013	174.496
0.7	105	-0.674	-0.007	232.167	1.0	105	-0.711	-0.007	244.442
0.7	120	-0.740	-0.012	209.635	1.0	120	-0.778	-0.010	217.884
0.7	135	-0.775	-0.012	227.773	1.0	135	-0.831	-0.011	232.047
0.7	150	-0.808	-0.007	302.826	1.0	150	-0.892	-0.007	303.707
0.7	175	-0.932	-0.009	385.865	1.0	175	-1.056	-0.010	388.532
0.7	200	-1.104	-0.008	331.44	1.0	200	-1.254	-0.007	331.536
0.7	250	-1.380	-0.015	207.059	1.0	250	-1.566	-0.014	206.238
0.7	300	-1.609	-0.012	113.791	1.0	300	-1.846	-0.013	113.462
0.7	400	-1.830	0.007	32.959	1.0	400	-2.121	0.003	32.959

Table 5.5. Attenuation functional at 2.0, 3.0, 4.0, and 6.0 Hz for Band-Pass filtered. The columns give values of frequency (first and sixth columns), hypocentral distance (second and seventh columns), attenuation D(r,f) at a reference distance of 40 km (third and eighth columns), associated error bar (fourth and ninth columns) and number of observations (fifth and tenth columns).

Eastern Turkey Filtered Velocity (D(r))									
2.0	10	0.948	-0.001	15.696	3.0	10	0.997	0.005	15.114
2.0	20	0.532	-0.001	35.666	3.0	20	0.564	0.004	42.912
2.0	30	0.240	0.001	50.204	3.0	30	0.257	0.002	54.108
2.0	40	0.000	0.000	62.373	3.0	40	0.000	0.000	65.244
2.0	50	-0.207	0.004	187.363	3.0	50	-0.208	0.008	194.103
2.0	75	-0.516	-0.004	206.263	3.0	75	-0.537	0.000	208.463
2.0	90	-0.663	-0.002	182.579	3.0	90	-0.719	0.001	183.201
2.0	105	-0.761	0.002	247.56	3.0	105	-0.851	0.005	247.135
2.0	120	-0.862	-0.001	218.815	3.0	120	-0.975	0.004	218.24
2.0	135	-0.957	-0.001	232.734	3.0	135	-1.111	0.001	232.734
2.0	150	-1.085	0.001	301.528	3.0	150	-1.259	0.004	299.261
2.0	175	-1.308	-0.002	385.199	3.0	175	-1.504	0.001	381.215
2.0	200	-1.565	0.003	329.275	3.0	200	-1.774	0.009	320.148
2.0	250	-1.945	-0.003	204.666	3.0	250	-2.199	0.002	189.377
2.0	300	-2.319	-0.005	113.12	3.0	300	-2.635	-0.003	99.961
2.0	400	-2.696	0.006	32.959	3.0	400	-3.086	0.002	30.786
4.0	10	1.088	0.012	15.117	6.0	10	1.187	0.017	13.623
4.0	20	0.625	0.008	42.712	6.0	20	0.691	0.012	43.948
4.0	30	0.287	0.004	55.092	6.0	30	0.320	0.006	58.741
4.0	40	0.000	0.000	65.457	6.0	40	0.000	0.000	67.066
4.0	50	-0.218	0.012	194.002	6.0	50	-0.237	0.016	193.264
4.0	75	-0.569	0.004	207.186	6.0	75	-0.613	0.009	205.519
4.0	90	-0.772	0.004	182.579	6.0	90	-0.857	0.006	177.457
4.0	105	-0.925	0.007	247.135	6.0	105	-1.042	0.006	240.971
4.0	120	-1.058	0.008	218.24	6.0	120	-1.170	0.013	216.921
4.0	135	-1.215	0.004	230.568	6.0	135	-1.339	0.009	223.776
4.0	150	-1.376	0.008	291.472	6.0	150	-1.526	0.012	270.127
4.0	175	-1.640	0.003	373.974	6.0	175	-1.819	0.008	335.23
4.0	200	-1.926	0.012	307.778	6.0	200	-2.130	0.012	265.425
4.0	250	-2.363	0.006	170.936	6.0	250	-2.541	0.004	122.17
4.0	300	-2.815	-0.001	88.928	6.0	300	-2.908	0.007	62.471
4.0	400	-3.292	0.001	25.825	6.0	400	-3.293	0.015	17.29

Table 5.6. Attenuation functional at 8.0, and 10.0 Hz for Band-Pass filtered. The columns give values of frequency (first and sixth columns), hypocentral distance (second and seventh columns), attenuation D(r,f) at a reference distance of 40 km (third and eighth columns), associated error bar (fourth and ninth columns) and number of observations (fifth and tenth columns).

Eastern Turkey Filtered Velocity (D(r))									
8.0	10	1.298	0.022	14.93	10.0	10	1.319	0.018	15.509
8.0	20	0.765	0.015	43.387	10.0	20	0.779	0.012	44.645
8.0	30	0.357	0.007	58.073	10.0	30	0.364	0.006	58.236
8.0	40	0.000	0.000	65.988	10.0	40	0.000	0.000	65.988
8.0	50	-0.264	0.016	191.912	10.0	50	-0.282	0.016	191.554
8.0	75	-0.657	0.011	202.471	10.0	75	-0.695	0.010	197.669
8.0	90	-0.914	0.009	172.669	10.0	90	-0.976	0.006	161.741
8.0	105	-1.117	0.006	216.864	10.0	105	-1.193	0.003	197.303
8.0	120	-1.257	0.012	203.77	10.0	120	-1.328	0.011	189.44
8.0	135	-1.413	0.014	204.778	10.0	135	-1.462	0.018	183.393
8.0	150	-1.607	0.016	232.076	10.0	150	-1.661	0.015	197.641
8.0	175	-1.896	0.011	276.162	10.0	175	-1.928	0.008	217.419
8.0	200	-2.196	0.006	203.872	10.0	200	-2.184	0.000	149.395
8.0	250	-2.508	0.003	87.638	10.0	250	-2.405	0.004	58.286
8.0	300	-2.716	0.021	42.12	10.0	300	-2.529	0.025	32.333
8.0	400	-2.951	0.041	13.289	10.0	400	-2.680	0.049	10.449

5.1.3 Duration

The duration of strong ground motion can have a strong influence on earthquake damage. A ground motion with moderate amplitude but long duration can produce enough load reversals to cause substantial damage (Kramer, 1996). Properly studied observed ground motions enable us to characterize the distance and frequency band influence on duration. Duration is a function of the rupture and of the dispersion that elastic waves experience along source and receivers paths (Herrmann, 1985). Scattering also contributes to the increase in duration at increasing distances from the source. Dispersion redistributes the frequency content of the radiated spectrum (Malagnini, 1999) in time. As a result, the duration increases with increasing earthquake magnitude and distance. Various other estimates such as duration (T) are fully described in Kramer (1996). Only the strong-motion portion of the accelerogram is important for engineering purposes.

Figures 5.11, 5.12, and 5.13 show the observed durations of S-wave and coda at 0.3, 0.7, 1.0, 4.0, 6.0, and 10.0 Hz. It is seen that there is significant scatter at 0.3 and 0.7 Hz which decreased at higher frequencies. At higher frequencies though, small signals due to attenuation did not permit a reliable estimation of duration at large distances. To estimate the distance dependence of duration, we modeled it as a piecewise linear function of distance.

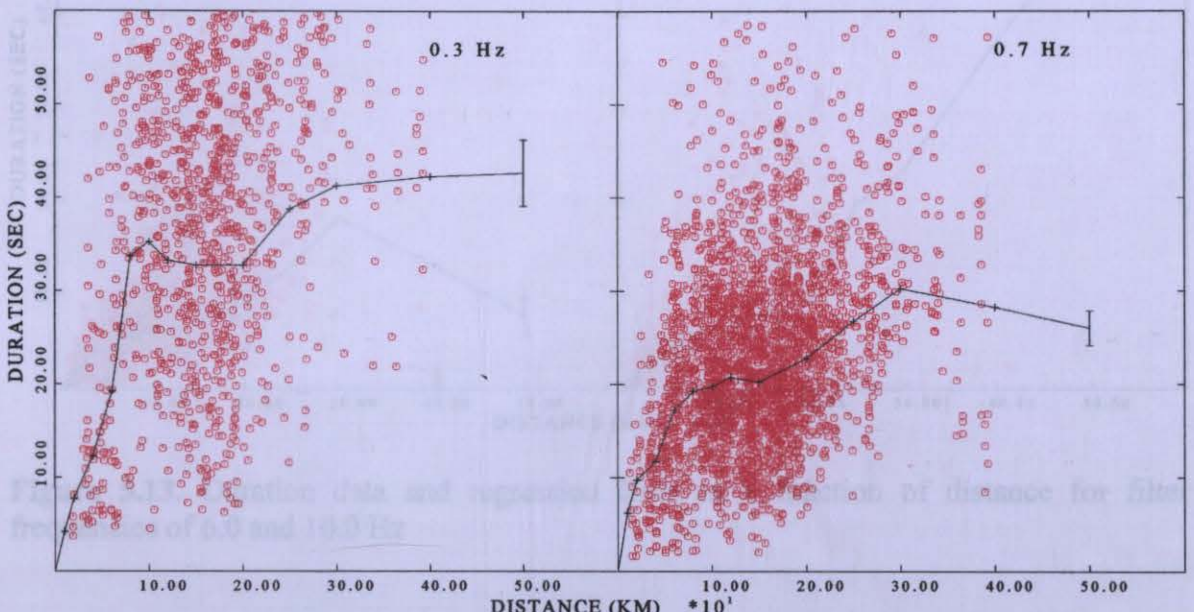

Figure 5.11. Duration data and regression lines as a function of distance for filter frequencies of 0.3 and 0.7 Hz

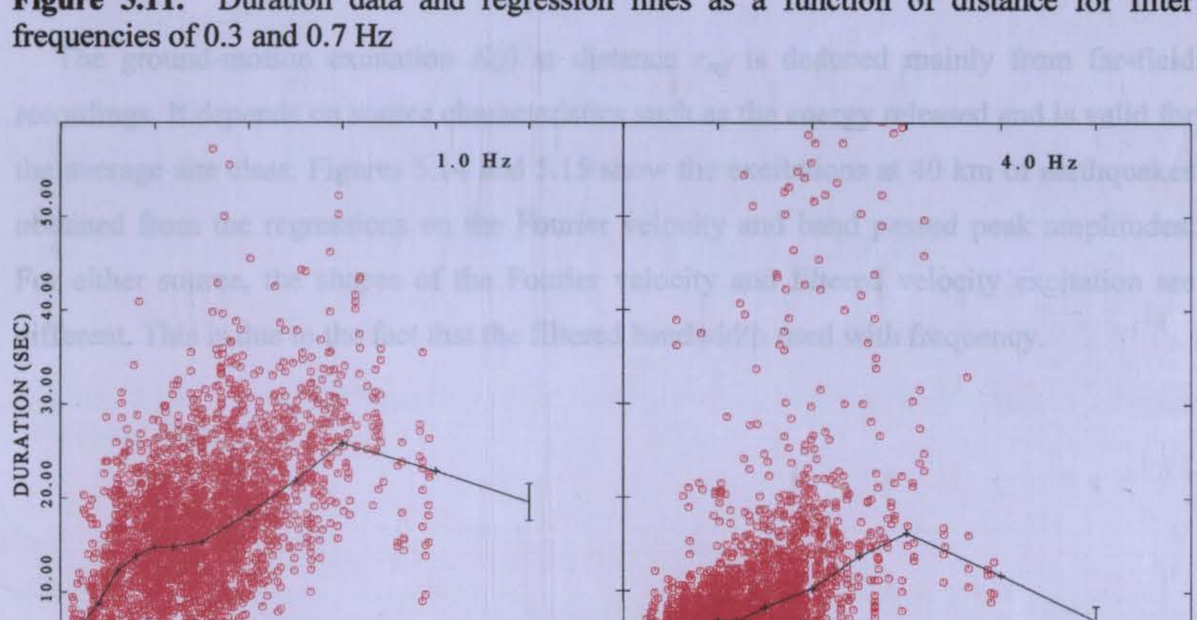

Figure 5.12. Duration data and regression lines as a function of distance for filter frequencies of 1.0 and 4.0 Hz

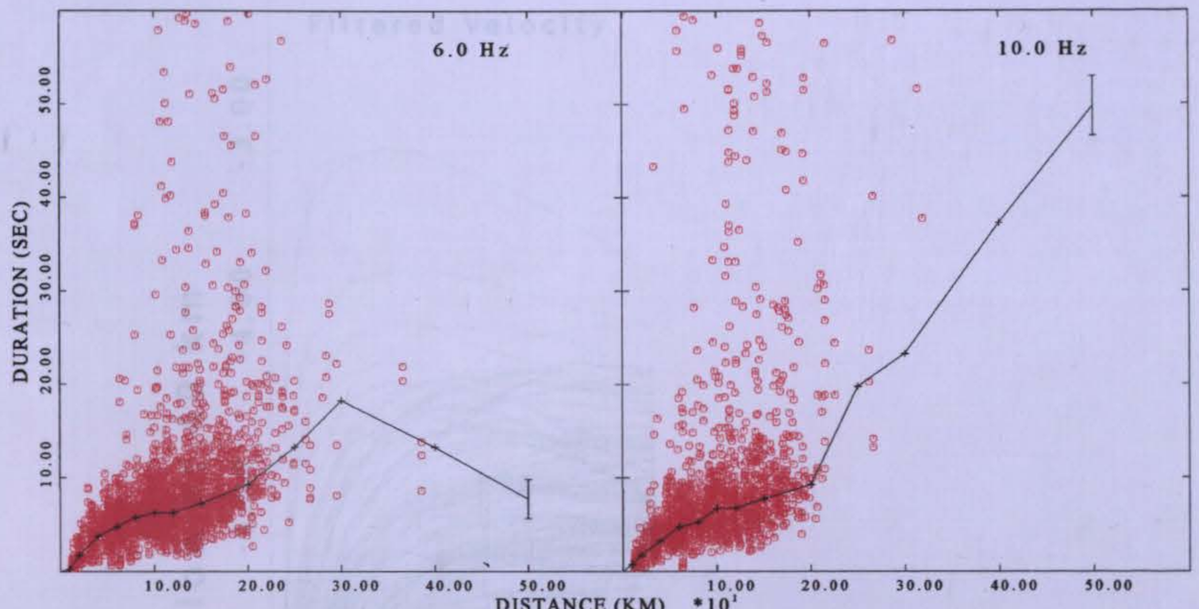

Figure 5.13. Duration data and regression lines as a function of distance for filter frequencies of 6.0 and 10.0 Hz

5.1.4 Excitation

The ground-motion excitation *E(f)* at distance r_{ref} is deduced mainly from far-field recordings. It depends on source characteristics such as the energy released and is valid for the average site class. Figures 5.14 and 5.15 show the excitations at 40 km of earthquakes obtained from the regressions on the Fourier velocity and band passed peak amplitudes. For either source, the shapes of the Fourier velocity and filtered velocity excitation are different. This is due to the fact that the filtered bandwidth used with frequency.

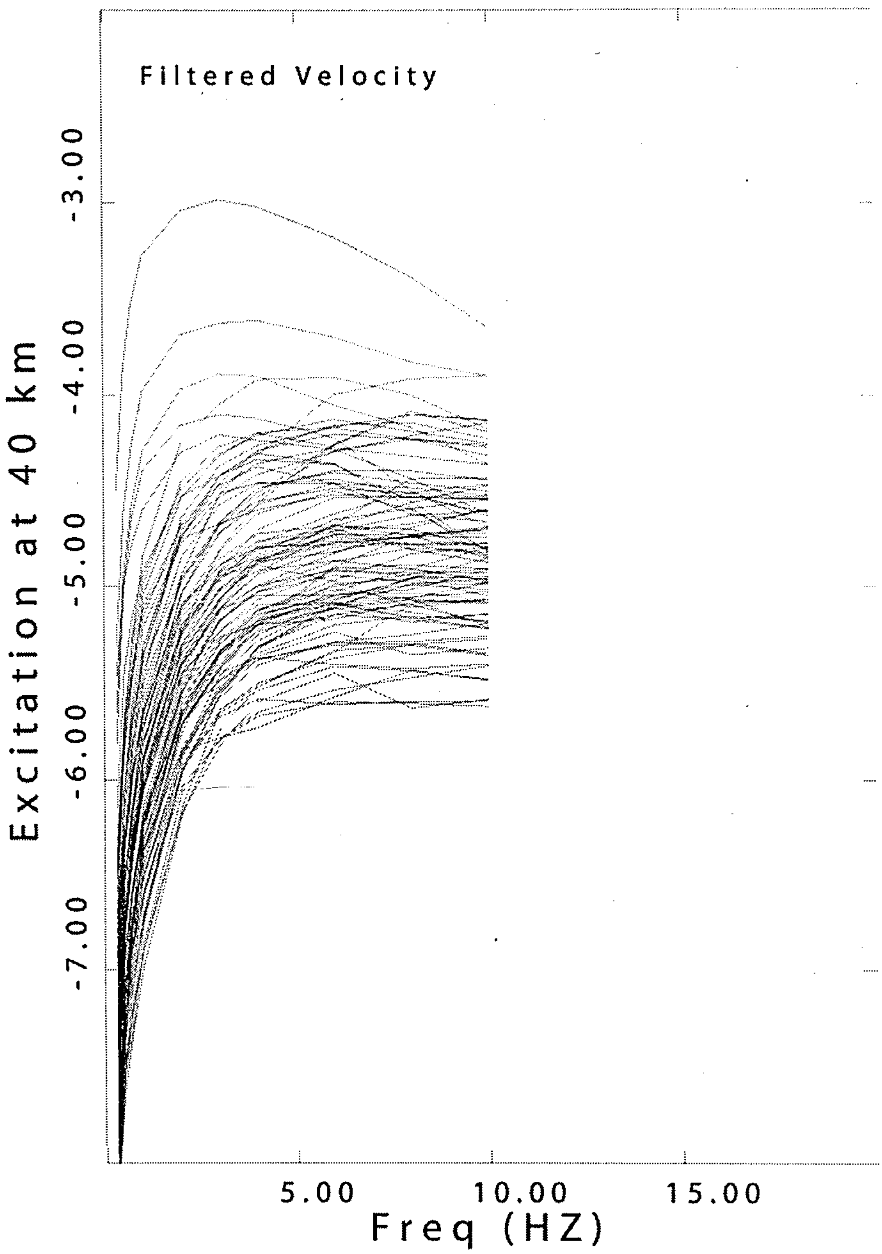

Figure 5.14. Inverted Filtered ground velocity excitation terms plotted on a linear frequency scale.

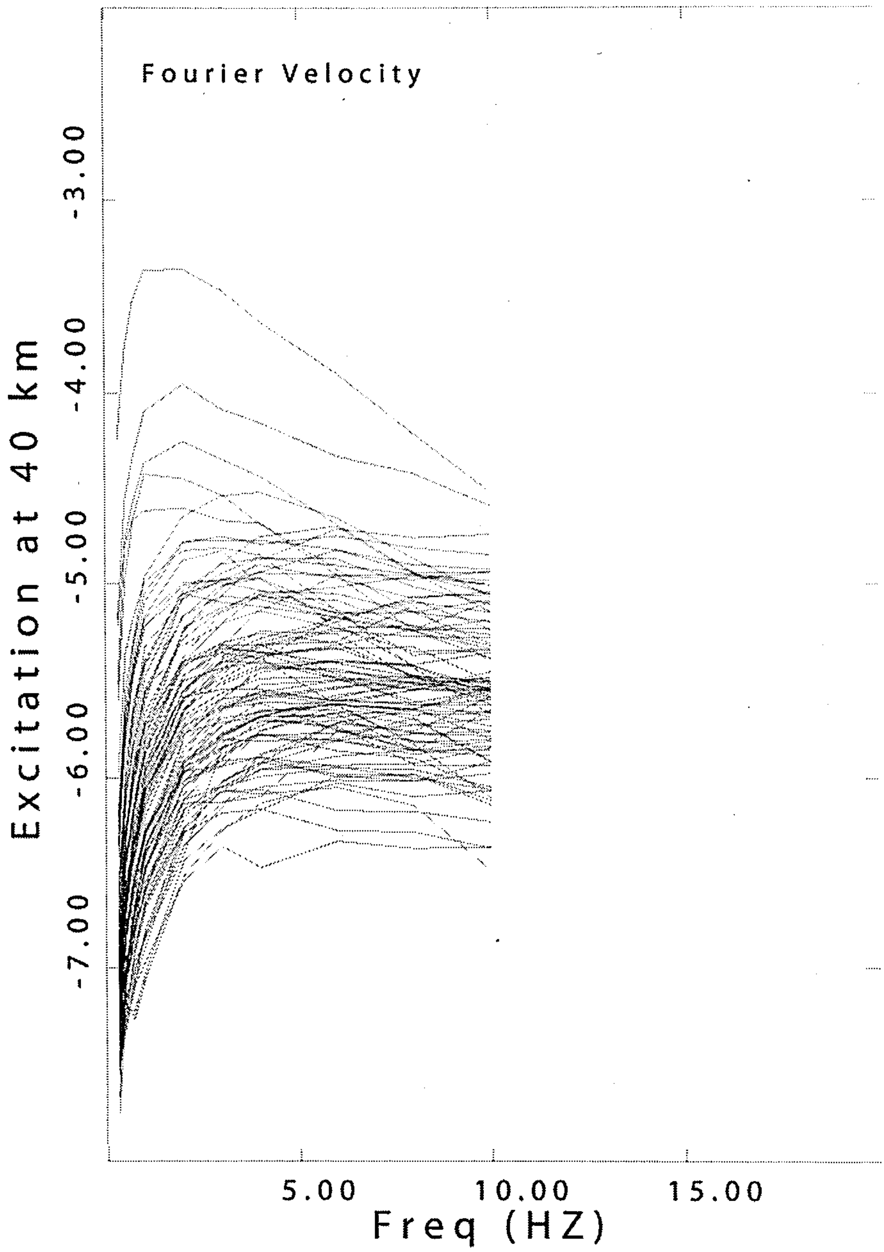

Figure 5.15. Inverted Fourier velocity excitation terms plotted on a linear frequency scale.

5.2 Modeling

The last stage of processing entailed the specification of a simpler parametric model that describes the observations.

5.2.1. Fourier Velocity Spectra Modeling

The predicted Fourier velocity spectra at a frequency *f* and a distance *r* is written as

$$a(r,f) = s(f,M_w)g(r)e^{-\pi fr/Q(f)\beta}V(f)e^{-\pi f\kappa} \tag{5.1}$$

where $a(r,f)$ is the observed Fourier velocity spectra, $s(f,M_w)$ is the source excitation as a function of a moment-magnitude, $g(r)$ is the geometrical spreading function, $Q(f)$ is the frequency dependent quality factor written as $Q_0(f/1.0)^\eta$, Q_0 is the quality factor at 1.0 Hz., $V(f)$ is a frequency dependent site amplification, and κ controls site dependent attenuation of high frequency .

Typically the form of $s(f,M_w)$ giving the Fourier velocity spectra at a distance of 1.0 km. From the source is

$$s(f,M_w) = K\frac{M_0}{4\pi\rho\beta^3 1000}(2\pi f)S(f) \tag{5.2}$$

where log M_0(nt.m) = 1.5M_w + 9.05 (Hanks and Kanamori, 1979), ρ(kg.m^{-3}) is the material density at the source, β(m/s) is the shear-wave velocity at the source, $S(f)$ is the omega-square displacement spectrum source model

$$S(f) = \frac{1}{1+(f/f_c)^2} \tag{5.3}$$

f_c can be defined in terms of the shearwave velocity at the source, β(m/s), the seismic moment, logM_0(nt.m) and the stress drop parameter, $\Delta\sigma$ (Mpa), by

$$f_c = 49\beta(\Delta\sigma / M_0)^{1/3} \tag{5.4}$$

and the constant *K* in equation 5.2 includes the composite factors of the radiation pattern, free-surface amplication and the partition of the initial shear-wave amplitude into the recorded component. We use the constant *K* and do not try to define the seperate effects. The units of velocity spectra $s(f,M_w)$ is meter. The geometrical spreading function $g(r)$ is dimensionless since it givens the reduction of amplitude relative to r = 1 km.

Using the regression results, we find that the following works fit in well both with the Fourier velocity and peak velocity $E(r)$:

A comparison of the regression parameters for the velocity spectra to terms of this formula shows the association:

$$10^E = s(f,M_w)g(r_{ref})e^{-\pi f r_{ref}/Q(f)\beta}\overline{V(f)e^{-\pi f \kappa}} \tag{5.5}$$

$$10^D = \frac{g(r)e^{-\pi f r/Q(f)\beta}}{g(r_{ref})e^{-\pi f r_{ref}/Q(f)\beta}} \tag{5.6}$$

$$10^{S_i} = \frac{V(f)e^{-\pi f \kappa}}{\overline{V(f)e^{-\pi f \kappa}}} \tag{5.7}$$

where $\overline{V(f)e^{-\pi f \kappa}}$ is the network average site effect (Herrmann, 2000).

From the second of these equations, we see that the $D(r,f)$ term is a function of the geometrical spreading $g(r)$ and the frequency dependent $Q(f)$. Thus simple forward modeling can provide possible candidates for these functions. The excitation term $E(f)$ depends on the source spectrum and the network average site effect.

5.2.2 Modeling Peak Time Domain Values

Random Vibration Theory (RVT) is a tool to estimate peak motion in a time series given the spectral amplitudes and signal duration (Cartwright and Longuet-Higgins, 1956). Boore (1983) applied this to the seismological problem of estimating response spectra and peak velocity and acceleration from earthquakes.

The mathematical development of Cartwright and Longuet-Higgins (1956) is complicated, but Boore (1996) provides software to perform the computations. A local adaption of random vibration theory for application to this study is called *rptcal*. Following Boore (1993), the site spectrum, which is a function of distance and frequency is used to compute the 0'th, 2'nd and 4'th spectral moments. Using the signal duration, which is a function of source size to reflect the rupture duration and distance to reflect the effect of propagation, the the RMS (root mean square) motion is computed by using Parseval's theorem. The RMS value is related to the peak value of motion by the η_{max} value. It was computed using the Cartwright and Longuet-Higgins (1956).

$$a_{\max} = \eta_{\max} a_{rms} \tag{5.8}$$

The signal duration enters into the peak motion estimation in two ways: in the estimation of the RMS value and in the definition of η_{max}.

Comparison of RVT model based predictions to observations requires that the source spectrum must be appropriate for the earthquakes used. Fortunately, the shape of the source spectrum is easy to define in our frequency range for the small earthquakes that we use. Thus the modeling of peak time domain motions builds upon the *g(r)* and *Q(f)* that estimated from the Fourier velocity spectra modeling and relies heavily on the duration function *T(r)*.

5.2.3 Propagation Parameters

We parameterize the geometrical spreading and attenuation functions to create a theoretical Fourier velocity spectra and filtered velocities of the propagation term. Results were modeled in terms of a simple function of geometric spreading and frequency dependent seismic attenuation. We found a geometrical spreading of

$$g(r)=\begin{Bmatrix} r^{-1} & r \le 40km \\ r^{0} & 40 \le r \le 100km \\ r^{-0.5} & 100 \le r \end{Bmatrix}$$

and an attenuation functional $Q(f)=50f^{0.75}$. We used a shear wave average velocity β of 3.5km/s. The geometrical spreading at distances shorter than the cross-over distance is related to the propagation of body waves and usually is assumed to be r^{-1}.

The attenuation functional $Q(f) = Q_0 f^{\eta}$ trades off with the geometrical spreading. The frequency dependent exponent, η, controls the separation between the different frequencies in the propagation functional. The attenuation functional *D(r,f)*, for peak filtered time domain and the Fourier amplitude were compared (Figures 5.16 and 5.17).

Table 5.7 shows the propagation parameters used in model. The *Q(f)* value in Table 5.7 is from the peak filtered velocity data set.

Table 5.7. Propagation parameters of Model

	Model
Q(f)	$50f^{0.75}$
g(r)	$\begin{Bmatrix} r^{-1} & r \le 40km \\ r^{0} & 40 \le r \le 100km \\ r^{-0.5} & 100 \le r \end{Bmatrix}$
κ_{eff}	0.035
$\Delta\sigma$	100 bars
ρ	2.8 g/cm^3
β	3.5 km/s

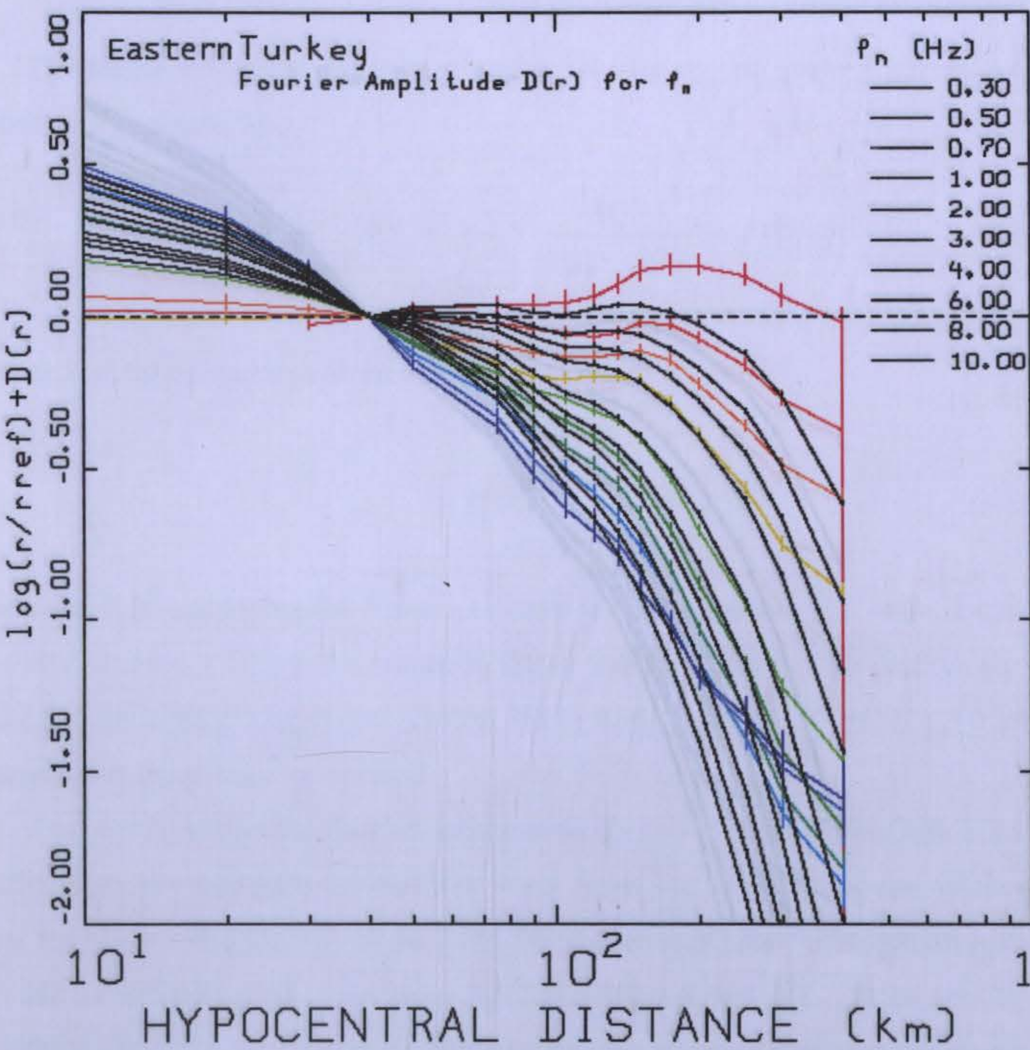

Figure 5.16. Attenuation functional $D(r,r_{ref},f)$ obtained from the regression of the Fourier amplitudes at the frequencies of 0.3, 0.5, 0.7, 1.0, 2.0, 3.0, 4.0, 6.0, 8.0, and 10.0 Hz that are shown by colored lines. Black lines represent theoretical predictions obtained after a trial-and-error modeling of the empirical (color) curves. The reference hypocentral distance is 40 km.

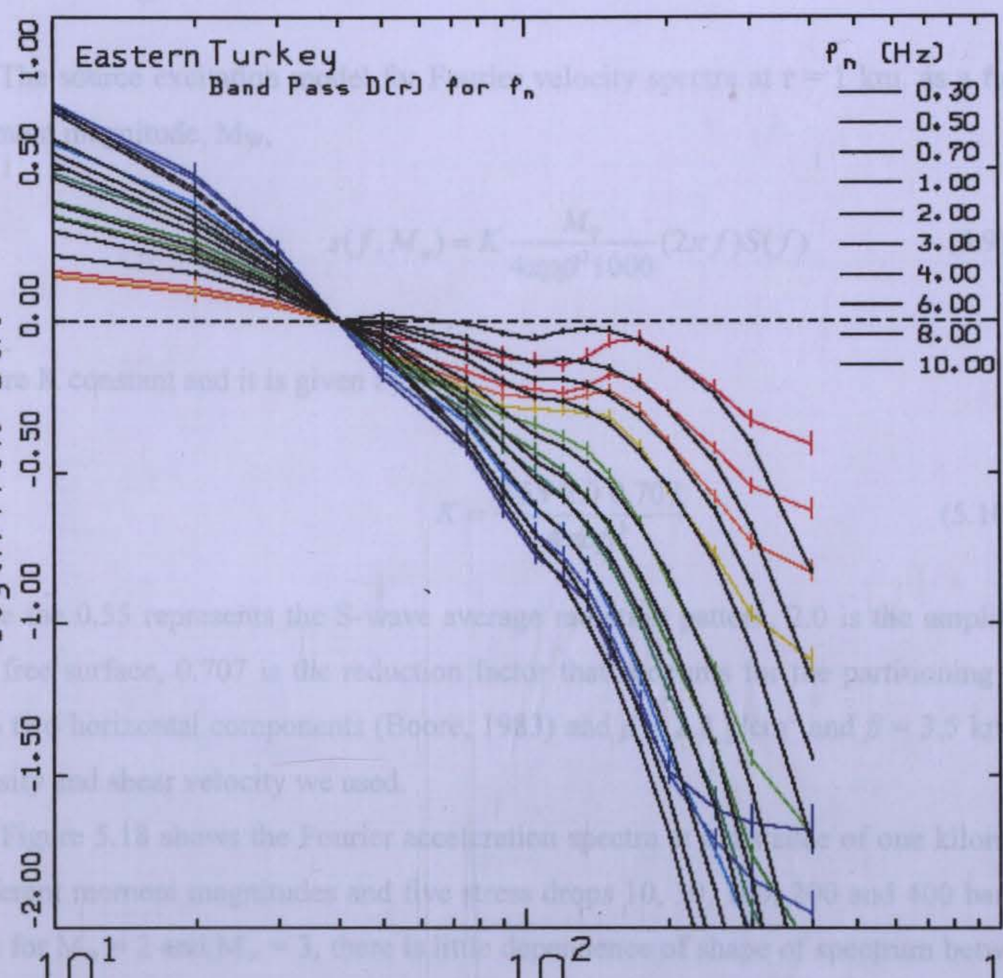

Figure 5.17. Attenuation functional D(r,rref,f) obtained from the regression of the filtered velocities at the frequencies of 0.3, 0.5, 0.7, 1.0, 2.0, 3.0, 4.0, 6.0, 8.0, and 10.0 Hz that are shown by colored lines. Black lines represent theoretical predictions obtained after a trial-and-error modeling of the empirical (color) curves. The reference hypocentral distance is 40km.

5.2.4 Modeling Source Excitation

The source excitation model for Fourier velocity spectra at r = 1 km. as a function of moment magnitude, M_W,

$$s(f, M_w) = K \frac{M_0}{4\pi\rho\beta^3 1000}(2\pi f)S(f) \tag{5.9}$$

where K constant and it is given by,

$$K = \frac{0.55\ 2.0\ 0.707}{4\pi\rho\beta^3} \tag{5.10}$$

Here the 0.55 represents the S-wave average radiation pattern, 2.0 is the amplification at the free surface, 0.707 is the reduction factor that accounts for the partitioning of energy into two horizontal components (Boore, 1983) and ρ = 2.8 g/cm^3 and β = 3.5 km/s are the density and shear velocity we used.

Figure 5.18 shows the Fourier acceleration spectra at a distance of one kilometer for 6 different moment magnitudes and five stress drops 10, 30, 100, 200 and 400 bars. We see that for $M_W = 2$ and $M_W = 3$, there is little dependence of shape of spectrum between 1 and 10 Hz as a function of stress drop for 100, 200 and 300 bars. Since we do not know anything about the local site conditions, we use the effective κ, κ_{eff} for the composite effect of network average site amplification, $V(f)$, and κ which we define as

$$e^{-\pi\kappa_{eff} f} = \overline{V(f)e^{-\pi\kappa f}} \tag{5.11}$$

Because the excitation for small events recorded at 40 km depends only on Q(f) and the κ_{eff} and not on the stress drop, studying small earthquakes enables us to estimate the site effect without worrying about the unknown source spectrum scaling. From our spectral model, I kept the V(f) = 1 and varied κ_{eff} to fit small earthquake spectra. A κ_{eff} = 0.035 sec, was selected, and it was shown in the propagation parameters in table 5.7. Linear frequency plots demonstrate good fit for small earthquakes. (Figure 5.19 and Figure 5.20)

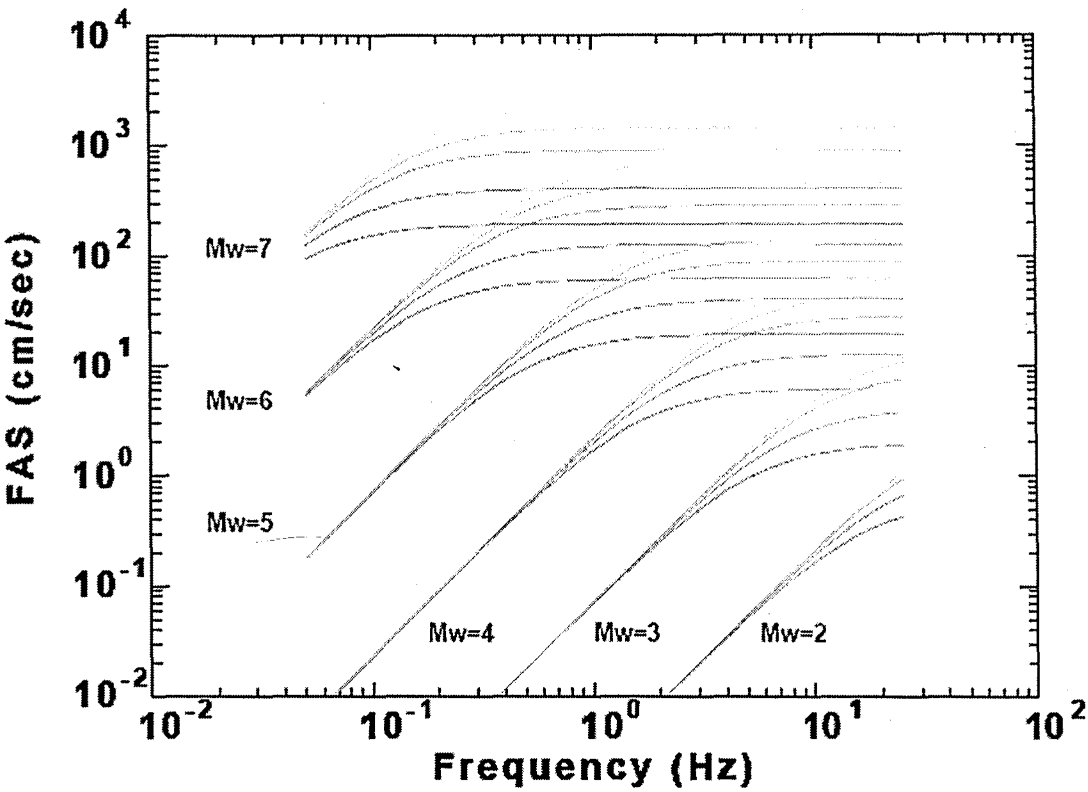

Figure 5.18. Fourier acceleration spectra at a distance 1 km as a function of M_w for stress drop 10, 30, 100, 200 and 400 bars. Dark and lightest line indicate 10 and 400 bars. The different M_w are indicated by the different low frequency asymptotics. For a given M_w, the high frequency level varies as $\Delta\sigma$.

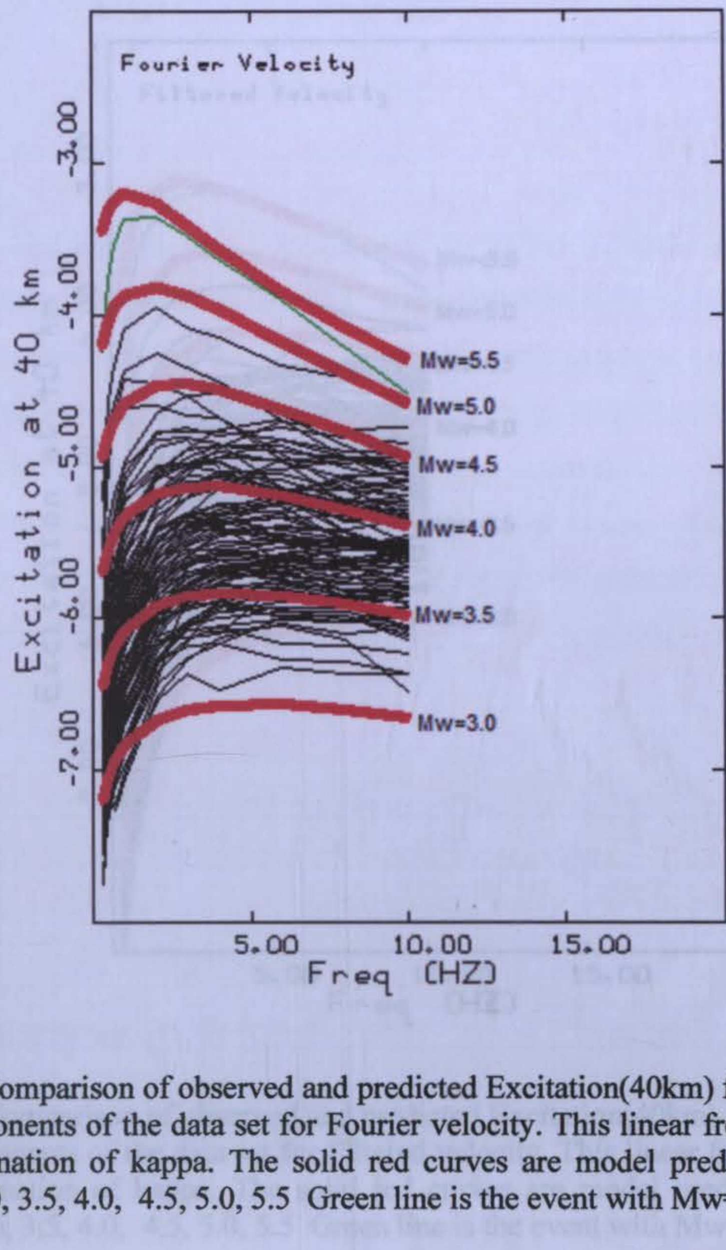

Figure 5.19. Comparison of observed and predicted Excitation(40km) for the regression of all three components of the data set for Fourier velocity. This linear frequency plot assists in the determination of kappa. The solid red curves are model predictions for moment magnitudes 3.0, 3.5, 4.0, 4.5, 5.0, 5.5 Green line is the event with Mw= 5.5 (Senkaya)

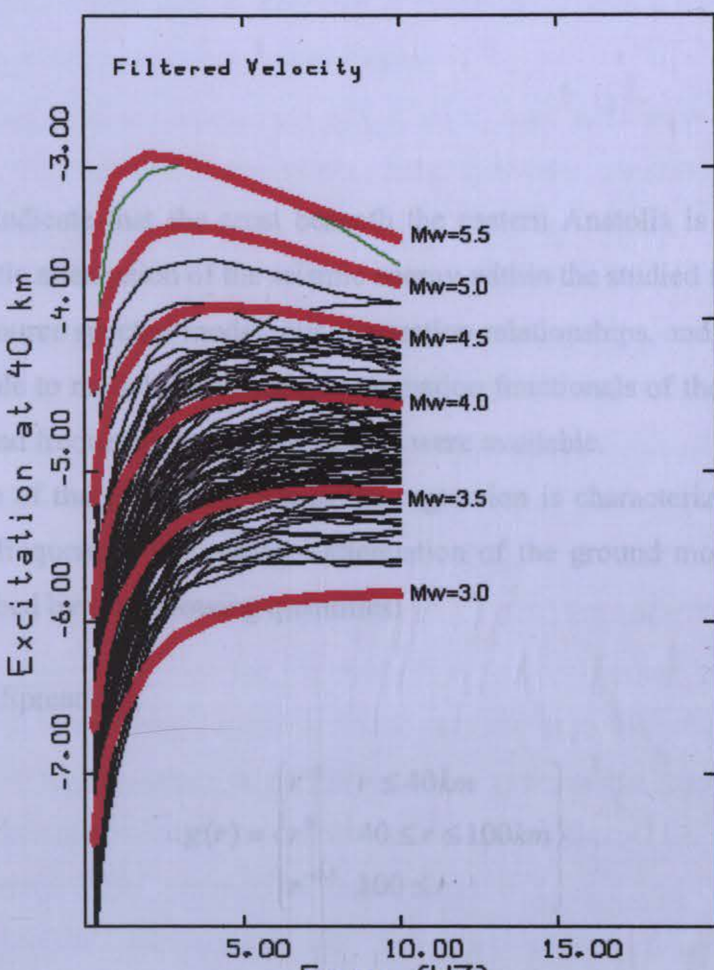

Figure 5.20. Comparison of observed and predicted Excitation(40km) for the regression of all three components of the data set for Filtered velocity. This linear frequency plot assists in the determination of kappa. The solid red curves are model predictions for moment magnitudes 3.0, 3.5, 4.0, 4.5, 5.0, 5.5 Green line is the event with Mw= 5.5 (Senkaya)

6. DISCUSSION AND CONCLUSIONS

6.1 Results

Our results indicate that the crust beneath the eastern Anatolia is characterized by a very high anelastic attenuation of the seismic energy within the studied frequency range.

By using a source spectral model, our attenuation relationships, and the RVT statistical tool, we were able to model the empirical attenuation functionals of the region, within the entire distance and frequency ranges where data were available.

The duration of the ground motion in the regression is characterized by a significant dependence on frequency. The regional attenuation of the ground motion in the Eastern Turkey is described by the following quantities:

Geometrical Spreading:

$$g(r)=\begin{Bmatrix} r^{-1} & r\leq 40km \\ r^{0} & 40\leq r\leq 100km \\ r^{-0.5} & 100\leq r \end{Bmatrix}$$

Anelastic attenuation:

$$Q(f)=50f^{0.75} \text{ and } \kappa_{eff}=0.035$$

6.2 Discussion

Regional ground motion scaling for Eastern Turkey is studied in this thesis. This study analyzed 100 earthquakes and nearly 3000 waveforms from 29 stations in the range of 10-400 km epicentral distance. Three component data from ETSE network used to obtain and quantify the regional attenuation ground motion.

Comparison of two regressions shows that both of regression results display consistent in shape. Random vibration theory used to obtain estimates of the peak ground motion in the time domain.

It was noted that for long distances the prediction may be inaccurate due to lack of observations. Selected low Q(f) is expected in tectonically active regions, and this Q(f) value is an average estimate over the entire region.

Different tectonic environments may reflect significant differences in the propagation characterization. Comparing our results with Italy, Germany, Mexico, and Central United States, we found higher ground motion attenuation in eastern Turkey.

Eastern Turkey is characterized by a low Q_0 compared to other regions in the world, and our results is smilar to Erzincan area studied with the same approach (Akinci,. 2001).

However due to the high frequency dependence $\eta = 0.75$, attenuation at higher frequencies does not differ much from that of lower frequencies as is the case of the Appenies in Central Italy. Malagnini et al. (2000a) studied the regional attenuation along the Appenies, and they found an attenuation of $Q(f) = 130f^{0.10}$ combined with a geometrical spreading, $r^{-0.9}$ for $r \leq 50$km, r^0 for $50 \leq r \leq 80$ km and $r^{-0.5}$ for $r \geq 80$ km. For low frequencies (0.3 to 1 Hz) the attenuation in eastern Turkey is higher than other regions, for higher frequencies the attenuation is very smilar to the Italian region.

In the Erzincan region Akinci et al., (2001) found geometrical spreading $r^{-1.1}$ for $r \leq 25$ km, and $r^{-0.5}$ for larger distances. An extremely low quality factor, $Q(f) = 40f^{0.45}$ is used to describe the anelastic crustal attenuation in the region.

We have obtained the crustal and the near surface attenuation coefficients independently from the source sizes and from the site characteristics; these parameters are very important in terms of seismic risk assessment and future studies can focus on the scaling of ground motion with earthquake size in this region.

Anelastic or intrinsic attenuation is affected from thermal and scattering processes. The scattering deflects and redistributes amounts of energy in the direct wave when it propagates through the heterogeneous medium, distributing it into the seismic coda. The combined effect of anelastic attenuation and scattering alter its shape by reducing high frequencies more rapidly with distance than lower frequencies. Thus, high attenuation in eastern Turkey can be due to partial melt within the uppermost mantle or hetereogenities in the crust.

REFERENCES

Aki, K., 1980. Scattering and attenuation of shear waves in the lithosphere, *J. Geophys. Res.*, 85, 6496-6504.

Akinci, A., L. Malagnini, N. A. Pino, L. Scognamiglio, R. B. Hermann, and H. Eyidogan (2001). High-frequency ground motion in the Erzincan region. Turkey: inferences from small earthquakes, *Bull. Seism. Soc. Am.* **91,** 1446–1455.

Allen, C., Geological criteria for evaluating seismicity, *Geol. Soc. Am. Bul.*, 86, 1041–1057, 1975.

Al-Lazki, A., D. Seber, E. Sandvol, N. Turkelli, R. Mohamad, and M. Barazangi, Tomographic Pn velocity and anisotropy structure beneath the Anatolian plateau (eastern Turkey) and the surrounding regions; *Geophys. Res. Lett.*, doi:10.1029/2003GL017391, 2003.

Ambraseys, N. N., Some characteristic features of the North Anatolian fault zone, *Tectonophysics*, 9, 143–165, 1970.

Ambraseys, N. N., K. A. Simpson, and J. J. Bommer (1996). Prediction of horizontal response spectra in Europe, *Earthquake Eng. Struct. Dyn.* 25, 371–400.

Anderson, J. G., and Y. Lei (1994). Nonparametric description of peak acceleration as a function of magnitude, distance, and site in Guerrero, Mexico, *Bull. Seism. Soc. Am.* 84, 1003–1017.

Atkinson, G. M., and D. M. Boore (1995). Ground-motion relations for eastern North America, *Bull. Seism. Soc. Am.* 85, 17–30.

Atkinson, G. M., and W. Silva (1997). An empirical study of earthquake source spectra for Californian earthquakes, *Bull. Seism. Soc. Am.* 87, 97–113.

Atkinson, G. and R. Mereu (1992). The shape of ground motion attenuation curves in southeastern Canada. *Bull. Seism. Soc. Am.*, 82, 2014-2031.

Barka, A., and K. Kadinsky-Cade, Strike-slip fault geometry in Turkey and its influence on earthquake activity, *Tectonics*, 7, 663– 684, 1988.

Bay, F., D. Fah, L. Malagnini, and D. Giardini (2003). Spectral Shear-Wave Ground-Motion Scaling in Switzerland, *Bull. Seism. Soc. Am.* 93, 414-429.

Boore, D. (1983). Stochastic simulation of high-frequency ground motions based on seismological models of the radiated spectra. *Bull. Seism. Soc. Am.*, 73, 1865-1894.

Boore, D. M., and W. B. Joyner (1997). Site amplification for generic rock sites, *Bull. Seism. Soc. Am.* 87, 327–341.

Boore, D.M. and Joyner, W.B. (1991). Estimation of Ground Motion at Deep-soil Sites in Eastern North America. *Bull. Seism. Soc. Am.*, 81, 2167-2185.

Campbell, K. W. (1997). Empirical near-source attenuation relationships for horizontal and vertical components of peak ground acceleration, peak ground velocity, and pseudoabsolute acceleration response spectra, *Seism. Res. Lett.* 68, 154–179.

Cartwright, D. E., and M. S. Longuet-Higgins (1956). The statistical distribution of the maxima of a random function, *Proc. R. Soc. London* A237, 212–232.

Dewey, J. F., and A. M. C. Sengor, Aegean and surroundings regions: Complex multiplate and continuum tectonics in a convergent zone, *Geolog. Soc. Of Amer. Bull.*, 90, 84–92, 1979.

Frankel, A., A. McGarr, J. Bicknell, J. Mori, L. Seeber, and E. Cranswick, Attenuation of high-frequency shear waves in the crust: measurements from New York state, South Africa and, southern California, *J. Geophys. Res.*, 95, 17441-17457, 1990.

Gok, R., N. Turkelli, E. Sandvol, D. Seber, and M. Barazangi, Regional wave propagation in Turkey and surrounding regions, *Geophysical Research Letters*, 27(3), 429- 432, 2000.

Gurbuz, C., N. Turkelli, T. Bekler, R. Gok, E. Sandvol, D. Seber, and M. Barazangi, Location and calibration using eastern Turkey broadband seismic network: Analysis of the Agari Dam explosion, *Bull. Seism. Soc. Amer.*, in review, 2003.

Harmsen, S. (1997). Estimating the diminution of shear-wave amplitude with distance: application to the Los Angeles, California, urban area, *Bull. Seism. Soc. Am.* 87, 888–903.

Herrmann, R. B. (1985). An extension of RVT estimates of strong ground motion to large distances, *Bull. Seism. Soc. Am.* 75, 1447–1453.

Herrmann, R. B. (2000). Comparative ground motion studies, *USGS Award* Number: 1434-HQ-97-GR03090.

Hempton, M. R., Structure and morphology of the East Anatolian Transform fault zone near Lake Hazar, southeastern Turkey, *Geol. Soc. Of Amer. Bull.*, 96, 233–243, 1985.

Jackson, J. A., and D. McKenzie, The relationship between plate motions and seismic moment tensors, and the rates of active deformation in the Mediterranean and Middle East, *Geophys. J.*, 93, 45- 73, 1988.

Jeon, Y.-S. (2000). High-frequency earthquake ground motion scaling in Utah, *Master's Thesis*, Saint Louis University, 106 pp.

Karapetian, S.G., R.T. Jrbashian, and A.K. Mnatsakanian, Late collision rhyolitic volcanism in the north-eastern part of the Armenian Highland, *J. Volc. Geotherm. Res.*, 112 (1-4), 189-220, 2001.

Keskin, M., J. A. Pearce, and J. G. Mitchell, Volcano-stratigraphy and geochemistry of collision-related volcanism on the Erzurum-Kars Plateau, North Eastern Turkey, *J. Volcanol. Geotherm. Res.*, 85, 355- 404, 1998.

Keskin, M., Magma generation by slab steepening and breakoff beneath a subduction-accreation complex: An alternative model for collision-related volcanism in Eastern Anatolia, Turkey, *Geophys. Res. Lett.*, 30(24), 8046, doi:10.1029/2003GL018019,2003.

Kramer, S. L. (1996). *Geotechnical Earthquake Engineering*, Prentice Hall, Upper Saddle River, NJ.

Malagnini, L. (1999). Ground motion scaling in Italy and Germany, *Ph.D. Dissertation*, Saint Louis University, Saint Louis, Missouri.

Malagnini, L., R. B. Hermann, and M. Di Bona (2000a). Ground-motion scaling in the Apennines (Italy), *Bull. Seism. Soc. Am.* 90, 1062–1081.

McClusky, S., S. Balassanian, A. Barka, C. Demir, S. Ergintav, I. Georgiev, O. Gurkan, M. Hamburger, K. Hurst, H. Kahle, K. Kastens, G. Kekelidze, R. King, V. Kotzev, O. Lenk, S. Mahmoud, A. Mishin, M. Nadariya, A. Ouzounis, D. Paradissis, Y. Peter, M. Prilepin, R. Reilinger, I. Sanli, H. Seeger, A. Tealeb, M. N. Toksoz, and G. Veis, GPS constraints on plate motion and deformation in the eastern Mediterranean: Implications for plate dynamics, *Journal of Geophysical Research*, 105, 5695–5719, 2000.

McKenzie, D., Active tectonics of the Mediterranean region, Geophys. *J. R. Astr. Soc.*, 30(2), 109- 185, 1972.

Raoof, M., R. B. Hermann, and L. Malagnini (1999). Attenuation and excitation of three-component ground motion in southern California, *Bull. Seism. Soc. Am.* 89, 888–902.

Sadigh, K., C.-Y. Chang, J. A. Egan, F. Makdisi, and R. R. Youngs (1997). Attenuation relationships for shallow crustal earthquakes based on California strong motion data, *Seism. Res. Lett.* 68, 180–189.

Sandvol, E., N. Turkelli, and M. Barazangi, The Eastern Turkey Seismic Experiment: The study of a young continent-continent collision, *Geophys. Res. Lett.*, 30(24), 8038, doi:10.1029/2003GL018912, 2003.

Sengor, A. M. C., and W. S. F. Kidd, The post-collisional tectonics of the Turkish-Iranian Plateau and a comparison with Tibet, *Tectonophysics*, 55, 361- 376, 1979.

Sengor, A. M. C., S. Ozeren, E. Zor, and T. Genc, East Anatolian high plateau as a mantle-supported, N-S shortened domal structure, *Geophys. Res. Lett.*, 30(24), 8045, doi:10.1029/2003GL017858, 2003.

Topuz, G., R. Altherr, A. Kalt, M. Satör, O. Werner, and W.H. Schwarz, Aluminous granulites from the Pulur complex, NE Turkey: a case of partial melting, efficient melt extraction and crystallization, *Lithos*, 72, 183-207, 2004.

Toro, G.R. and R.K. McGuire (1987). An investigation into earthquake ground motion characteristics in eastern North America. *Bull. Seism. Soc. Am.*, 77(2), 468-489.

Turkelli, N., E. Sandvol, E. Zor, R. Gok, T. Bekler, A. Al-Lazki, H. Karabulut, S. Kuleli, T. Eken, C. Gurbuz, S. Bayraktutan, D. Seber, M. Barazangi, Seismogenic Zones in Eastern Turkey, *Geophys. Res. Lett.*, 30(24), 8039, doi: 10.1029/2003GL018023, 2003

Yilmaz, Y., O. Tuysuz, E. Yigitbas, S.C. Genc, and A.M.C. Sengor, Geology and tectonic evolution of the Pontides, in Regional and Petroleum geology of the Black Sea and Surrounding Region, Ed. A.G. Robinson, *AAPG Memoir* 68, 183-226, 1997.

Yazd, M. R. S. (1993). Ground motion studies in the Southern Great Basin of Nevada and California, *Ph.D. Thesis*, Saint Louis University.

Zor, E., Gurbuz, C., Turkelli, N., Sandvol, E., Seber, D. and Barazangi, M., The crustal structure of the East Anatolian Plateau from receiver functions, *Geophys. Res. Lett.*, 30(24), 8044, doi:10.1029/2003GL018192, 2003.